NBSIR 77-1208

NBS Space Processing Research

E. Passaglia, R. L. Parker

Institute for Materials Research
National Bureau of Standards
Washington, D. C. 20234
Phone: (301) 921-2822

February 1977

Annual Report
For the Period 1 January 1976 - 31 December 1976
NASA Government Order H-19333B

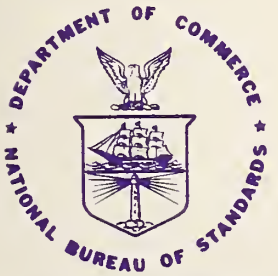

U. S. DEPARTMENT OF COMMERCE
NATIONAL BUREAU OF STANDARDS

NBSIR 77-1208

NBS SPACE PROCESSING RESEARCH

E. Passaglia, R. L. Parker

Institute for Materials Research
National Bureau of Standards
Washington, D. C. 20234
Phone: (301) 921-2822

February 1977

Annual Report
For the Period 1 January 1976 - 31 December 1976
NASA Government Order H-19333B

This report was prepared by the National Bureau of Standards
under Government Order H-19333B - NBS Space Processing Research,
for the Advanced Missions Program of the National Aeronautics
and Space Administration

U.S. DEPARTMENT OF COMMERCE, Juanita M. Kreps, *Secretary*

Dr. Betsy Ancker-Johnson, *Assistant Secretary for Science and Technology*

NATIONAL BUREAU OF STANDARDS, Ernest Ambler, *Acting Director*

TABLE OF CONTENTS

Page

Summary 1-2

Task 1 - CRYSTAL PERFECTION IN CZOCHRALSKI GROWTH -- NICKEL by
M. Kuriyama, W. J. Boettinger and H. E. Burdette..... 3-33

Task 2 - EVAPORATIVE PURIFICATION OF ULTRA-HIGH PURITY MATERIALS
Part A, by E. R. Plante..... 34-40
Part B, by W. J. Boettinger and F. S. Biancaniello..... 41-63

Task 3 - VAPOR TRANSPORT SYNTHESIS AND CRYSTAL GROWTH by
H. S. Parker..... 64-71

Task 4 - MELT SHAPE IN WEIGHTLESS CRYSTAL GROWTH by
S. R. Coriell, S. C. Hardy and M. R. Cordes..... 72-108

Task 5 - CONSULTING SUPPORT..... 109

Distribution List..... 110-111

National Bureau of Standards
Space Processing Research

Summary

This report describes NBS work for NASA in support of NASA's Space Processing Program covering the period January 1, 1976 - December 31, 1976. The objectives of the NBS program are to perform ground-based studies (and, where appropriate, space-based studies) of those aspects of space that could possibly provide a unique environment for making materials more perfect or more pure. The approach taken deals primarily with experimental and theoretical studies of the possible effects of the absence of gravitational forces on those materials preparation processes where the presence of gravity may be important in reducing perfection or purity. The materials preparation processes studied comprise four tasks in the areas of crystal growth, purification and chemical processing. There is an additional task on consulting support.

The results obtained for each task are given in detailed summaries in the body of the report. Briefly, in Task 1 - Crystal Perfection in Czochralski Growth - large nickel single crystals have been grown having dislocation densities as low as 400 lines /cm^2 as assessed by x-ray dynamical diffraction techniques. In Task 2 - Evaporative Purification of Ultra-High Purity Materials - Part A - it was determined that the use of sessile drops as a means of support for the study of molten alumina places severe restrictions on the type and validity of the data that can be obtained in view of temperature measurement and control problems encountered. In Part B, rates of evaporative purification were determined for Nb-Mo and for Mo-Zr alloys at elevated temperatures using R.F. levitation of

molten drops. In Task 3 - Vapor Transport Synthesis and Crystal Growth - the growth of 1.5 cm diameter crystals of mercurous chloride crystals by a vapor Bridgman technique is described. In Task 4 - Melt Shape in Weightless Crystal Growth, thermocapillary forces on air bubbles in a viscous oil were measured, and the shape of axisymmetric liquid zones and their stability with respect to perturbations has been investigated numerically.

Task 1

Crystal Perfection in Czochralski Growth--Nickel

M. Kuriyama, W. J. Boettinger and H. E. Burdette

Metallurgy Division
Institute for Materials Research

Summary

To study the relationship between crystal growth conditions and resultant crystalline perfection, large nickel single crystals more than 12 cm long and 2 to 3 cm in diameter have been grown from the melt by the Czochralski method. Unlike semiconducting materials, one cannot easily thin metal crystals, without straining them, for the purpose of applying ordinary Lang topography with $\mu L \sim 1$ where kinematical scattering in imperfect crystals is a good approximation. This situation with metal crystals necessitates the use of dynamical diffraction effects in imperfect crystals to permit sample crystals to be thick enough to demonstrate their imperfections as in the bulk.

The crystal perfection of as-grown nickel single crystals has been assessed by x-ray dynamical diffraction topography with an asymmetrical (double) crystal topographic (ACT) camera. Transmission topographs were obtained from crystals of thickness ranging from 0.37 mm ($\mu L=18$) to 1.03 mm ($\mu L=52$) using {111}, (002) and (220) diffraction. The crystals grown under favorable conditions have shown strong anomalous transmission. The O-diffracted (transmitted) and the H-diffracted (Bragg-diffracted) beams display almost identical disruption images of crystal imperfections in the interior of the crystals. The types of

imperfection and the degree of crystal perfection will be sorted by a set of crystal growth parameters, such as seed orientation and rotation rate. In addition to the images of crystal imperfections, there are disruption images of 71° and 109° magnetic domain walls in the topographs.

In this work it has been found, as in previous works on copper, that nickel single crystals can be produced with perfection far better ($\lesssim$400 dislocation lines/cm^2) than the common level by controlling practical process parameters, such as the rotations of the seed and the melt, and the growth directions. However, more crucial factors influencing the ultimate level of crystal perfection are governed by some crystallographic effects closely related to the behavior of dislocations in grown crystals. Anisotropic and directional dependence of dislocation properties plays a significant role in improving the crystalline perfection above a certain level. Some factors which are required to obtain dislocation-free crystals will be discussed based on the present experimental results, along with some comments on crystal growth experiments in space.

Introduction

X-ray double crystal diffraction topography has recently been employed to establish the fact that crystal growth conditions play a significant role in producing large copper single crystals of high perfection from the melt by the Czochralski technique[1-5]. In particular, several interesting crystallographic effects, such as seed orientation and dislocation type, have been found to influence the

resultant crystalline perfection. However, these results alone are not sufficient to draw the conclusion that the observed effects take place in most metal crystals. Nickel has a face-centered cubic crystal structure like copper, while material properties such as dislocation mobility, stacking fault energy and dislocation velocities are considerably different from copper. We have thus extended our work to large nickel single crystals grown from the melt by the Czochralski technique.

Nickel is ferromagnetic. Production of highly perfect nickel single crystals certainly provides the opportunity to study magnetic domain configurations in the interior of bulk nickel crystals by x-ray dynamical diffraction topography. In the past most of the magnetic domain observations in the interior of metal crystals were restricted to iron crystals or iron-silicon crystals; thus this new opportunity with nickel will be quite significant in understanding the behavior of ferromagnetic domains and their walls in industrial applications of soft magnetic materials where the minimization of electric energy loss is an important problem.

When compared with iron, nickel has smaller saturation magnetization, larger magnetostriction and a substantially smaller magnetic anisotropy energy. Nickel crystals thus deviate more significantly from cubic symmetry than iron or iron-silicon crystals. The magnetic domain walls would be broader since the wall thickness is inversely proportional to the square root of the magnetic anisotropy energy[6]. These different magnetic properties may display diffraction phenomena in such a favorable way that one can approximate a real domain wall by

a simple mathematical model of crystal imperfections, to which a general dynamical diffraction theory[7-9] can be applied rather rigorously.

Experimental Procedures

At the current stage of crystal growth research, it is not only inevitable, but desirable to characterize growth conditions by a set of variables chosen from the simplest, most practical and controllable process parameters available. These variables are indeed related in a very complex manner to the independent physical and thermodynamic variables which truly describe a physical system consisting of a growing crystal and the melt. In spite of this complexity, those chosen process parameters can be considered as reasonable variables, only if they are capable of describing results with sufficient reproducibility. For a study of the relationship between crystal growth conditions and resultant crystalline perfection, the first task will therefore be to assess the crystal perfection nondestructively and accumulate these data under several fixed growth conditions for a check of reproducibility. In this work, we choose as principal variables the angular velocities of crucible and seed, bottlenecking, the pulling speed, diameter control during growth, and the effect of seed orientation. There are, of course, some other important variables such as temperature gradient and deviation of the rotations from axial symmetry. However, we assume in this work that they are fixed.

Large nickel single crystals were grown by the Czochralski technique from either polycrystalline or single crystal ([100], [110] and [111] grown directions) seeds in an argon atmosphere. The procedures

of nickel single crystal growth and sample preparation for x-ray diffraction topography have been described in detail previously[10]. Briefly, the melt and seed were rotated around a common axis in the same direction independently with different rotational speeds; the relative speed of rotation ranged from 0.1 to 4.0 rpm, as shown in Table I. Nickel of 99.99% purity was used as the melt charge. Crystal boules were initially narrowed down in one region, thus forming a "bottleneck." The grown crystals were about 12 to 16 cm long with diameters between 2.0 and 3.0 cm and with a bottleneck diameter, whenever achieved, of slightly less than 1 mm. The boules were oriented by the Laue method and sliced into discs with an acid saw. The discs were polished on an acid polishing wheel. The following chemical compositions were found to be most effective for the strain-free cutting and polishing of nickel samples: 45% nitric acid, 33% hydrochloric acid, 20% acetic acid and 2% ethyl alcohol (in volume percent). Among these, ethyl alcohol plays an important role in maintaining the solution in a highly volatile state. A freshly prepared solution should be used at all times. For the cutting the crystal boule should be heated to about 90°C to keep the cutting time reasonable. The discs have $(1\bar{1}0)$ planes as their parallel faces in this work.

X-ray diffraction topographs were taken in both the transmission and the surface reflection geometry with an asymmetric (double) crystal topographic (ACT) camera[1,2,11]. In the transmission geometry both the O-diffracted (transmitted) beam and the H-diffracted (Bragg-diffracted) beam are recorded simultaneously on the same nuclear plate. A high-resolution double-crystal scanning diffractometer (SCAD)[3] was used to

obtain the profiles and widths of rocking curves at various locations in the crystal. $CuK\alpha_1$ radiation was used throughout the present work. To avoid damage to the crystals caused by conventional measuring techniques, the thicknesses of the discs were determined by the anomalous transmission effect from the separation between the undiffracted and the transmitted (0-diffracted) beam in a manner described previously[3,4]. For the crystals used in this work the product of the ordinary linear absorption coefficient, $\mu = 49.6\ mm^{-1}$, and the thickness, L, ranges from 18 to 52. Topographs were taken using symmetric $(\bar{2}20)$ diffracting planes in the surface reflection geometry and (111) and $(11\bar{1})$ planes in the transmission geometry. Occasionally, (220), $(00\bar{2})$ and other {111} planes were used for transmission topographs; specific diffracting planes are listed for individual samples in Table I. Ilford L-4 nuclear[12] plates (50 μm emulsion thickness) were used for all topographs.* The rocking curves were obtained from these sample crystals with the SCAD for the $\bar{2}20$ diffracted beam in the surface reflection geometry and mostly for the $11\bar{1}$ beam in the transmission geometry, using silicon (220) in the surface reflection mode for the first crystal. These results are also listed in Table I. The rocking curve width in transmission becomes narrower for the same degree of perfection, when the crystal disc becomes thicker. The values of μL for each sample are therefore included in Table I.

*In the topographs black represents fewer photons except Figure 9 which is reversed.

Experimental Results

Figure 1 shows an example of crystal boules which demonstrate a successful bottleneck of less than 1 mm and diameter control at will by changing temperature in the melt. The lower part of the crystal boule represents the shape when the diameter was controlled to be constant during growth. Figure 2 shows a typical shape of crystal boules with a spiral growth form. This shape is to be contrasted with the usual cylindrical growth form shown in Fig. 1. The spiral growth form has been reproduced repeatedly whenever the difference between the seed and the crucible rotation speed, Δ, becomes less than 0.3 rpm with a pulling speed of 1 mm·min^{-1}. It has also been observed that Δ has a lower bound, perhaps $\sim$0.1 rpm for this growth form. When the pulling speed was reduced to 0.4 mm·min^{-1}, crystals grew in a regular cylindrical form even with a small value of Δ. In Table I, crystal boules grown with a spiral form are indicated by letter C. As shown later, the growth shape does not seem to affect resultant crystal perfection as much as the growth direction does.

The growth directions of the crystal boules grown with a polycrystalline seed were found to be very close to the [111] direction. It has also been confirmed that boules grown from oriented crystal seeds have the same crystallographic orientation as the seeds.

Figure 3 shows drastic changes in the gross aspects of crystal perfection as the crystal growth conditions vary. Figure 3a shows that the crystal was polycrystalline when a [110] oriented seed was used. Figure 3b indicates that the crystal consists of several grains whose

misorientations are within 100 seconds of arc; this crystal was grown from a [100] oriented seed. Figure 3c represents a typical surface topograph from crystals grown from a polycrystalline seed or a [111] oriented seed under poor diameter control; small angle grain boundaries are visible. Figure 3d is an example of surface reflection topographs obtained from crystals grown under satisfactory diameter control from either a polycrystalline or a [111] oriented seed. For all of these crystals the growth conditions characterized by the rotational speeds and the pulling speed are almost identical. These crystals have a successful bottleneck. As also seen in Table I, boules grown in either [100] or [110] direction are not as perfect as those grown from a polycrystalline or [111] seed.

When the gross aspects of crystal perfection shown in surface topographs surpass the level represented by Fig. 3b, crystals can display anomalous transmission. Figure 4 shows ACT transmission topographs of the O-diffracted and the H-diffracted beams from crystal #194231 grown from a [100] seed without a bottleneck and without diameter control. They show a multigrain structure. When crystals were grown under more favorable conditions from a polycrystalline or a [111] seed with a successful bottleneck and good diameter control, their transmission topographs displayed a prominent anomalous transmission effect with detailed dislocation arrangements. As shown in Fig. 5, an arrangement of Lomer-Cottrell sessile dislocations has been confirmed in several crystals grown under a condition similar to that for sample #280232. This arrangement has been observed in copper single crystals under certain growth conditions[4,5]. Figure 6 shows ACT $11\bar{1}$

transmission topographs obtained from sample #363232, in which very small angle grain boundaries, generally curved, are visible along with isolated dislocations. Figure 7 shows ACT $11\bar{1}$ transmission topographs from sample #310232, in which no small angle boundaries exist and isolated dislocation images are clearly visible. In both of these figures, the regular straight-line images correspond to ferromagnetic domain walls, as will be discussed in the next section.

As shown previously[1-3], spectroscopic data--namely, rocking curve widths--alone supply adequate information regarding the degree of crystal perfection in sample crystals. The value of each rocking curve width was measured as the full width at half maximum (FWHM) of each rocking curve or spectral profile. The crystals are considered to be more perfect, the smaller the observed width for the same μL-value. These results are listed in Table I. When crystal boules were grown without a bottleneck and without diameter control, they were so imperfect that spectroscopic data could not be obtained. It has also been found that sample crystals from the boules grown in [100] and [110] directions display such a broad diffraction profile that they are much less perfect than those grown from a polycrystalline or [111] seed. A possible effect of the growth direction will be discussed later, in particular concerning the [110] growth direction. By contrast, the failure of diameter control does not affect the resultant perfection as much as the other factors. However, the spectroscopic data suggest that the rocking curve widths are usually smaller, indicating more perfect crystals, if the diameter is controlled during the entire period of growth.

Conclusion and Discussion

a) Crystal Imperfections--dislocations and micro-subgrain boundaries

Although the ultimate goal of this type of work is to find the best growth condition for the production of crystals free of dislocations, it is important to characterize the nature of dislocations and imperfections in crystals grown under different conditions, particularly when the crystals become nearly perfect. Figure 5 implies, as in the growth process for copper,[4,5] that new dislocations are often created continuously during the growth, but they become immobile under particular growth conditions. This mechanism results in a more perfect crystal as a whole than under some other growth conditions.

It is known that the formation of grain boundaries is closely related to dislocations in the crystal. Figure 8 shows very-small-angle subgrain boundaries revealed in a surface reflection topograph. In contrast with ordinary subgrain boundaries, these should be called microsubgrain boundaries in which two adjacent domains are mutually tilted less than 500 seconds of arc. This crystal was grown in an unfavorable growth direction, [100]. By our standards, this crystal is quite imperfect, although each subgrain displays anomalous transmission, as shown in Fig. 4, indicating that this crystal is far more perfect than ordinary crystals. This topograph indicates an important feature in the relation between crystal perfection and growth conditions. In this surface topograph, the boundaries are shown as a black or white trace as a consequence of overlapping or separation of beams diffracted from different subgrains. These traces give a value of approximately 270 seconds of arc for mutual tilt of subgrains. The rotation axis of

the subgrain is found to be the growth axis. It should be noted also, in contrast with predictions of ordinary continuum crystal growth theories, that these boundaries are not straight lines, although many are close to ⟨111⟩ directions. This phenomenon may account for the reason why the growth directions other than [111] would not produce perfect crystals. A further study on this aspect will be published shortly elsewhere[13].

When crystals are grown under favorable growth conditions, they become highly perfect. Figure 9a and b demonstrate dislocation densities of about 400 lines/cm^2 or less. It has so far been confirmed that, whenever crystals were grown under the favorable conditions, dislocation densities seldom exceed 2000 lines/cm^2. These results are quite remarkable, if one takes into account the fact that nickel is a metal and these densities have been obtained in the as-grown state.

b) Ferromagnetic Domains and Their Walls

In the past, two attempts[14,15] were made to observe magnetic domains in nickel crystals with x-ray diffraction topography, while many extensive topographic studies[16-25] were carried out with Fe-Si and iron crystals. The primary difficulty of x-ray topographic observation of magnetic domains and domain walls in nickel crystals lies in the required degree of crystal perfection. As demonstrated in the previous section, it is now possible to achieve a sufficiently high level of crystal perfection in large nickel crystals grown by the Czochralski technique. There exist, in fact, extremely straight-line images along with rather random arrangements of crystal imperfection images in the transmission topographs as shown in Figs. 6 and 7. These straight-line

images usually form regular rectangular arrangements, and they disappear upon application of a magnetic field in one of easy magnetization directions ⟨111⟩ as shown previously[10,26]. It may be helpful for the identification of images to correlate crystallographic directions with the easy magnetization directions. The magnetization vectors in the sample crystals probably are the directions of easy magnetization ([111] and $[11\bar{1}]$) in the $(1\bar{1}0)$ plane which is parallel to the surfaces of all our crystal discs. In such crystals, 71° and 109° domain walls intersect the crystal surfaces in lines parallel to [001] and [110], respectively, while 180° walls intersect the crystal in lines parallel to [111] and $[11\bar{1}]$. An interesting topograph of oblique magnetic domain walls in the interior of the crystal is shown in Fig. 10. The success of direct observation of magnetic domain walls by x-ray topography is quite significant, since it will enable one to study the dynamic behavior of ferromagnetic domain walls under a varying magnetic field and to understand the mechanism of micro-eddy currents, and in turn, electric energy losses in industrial applications of soft magnetic materials. However, the x-ray topography study of magnetic domain walls in nickel crystals is beyond the scope of this report. Although detailed work on this aspect has been published elsewhere,[26-29] we will demonstrate a basic mechanism of magnetization in B-H curves by x-ray topography through Fig. 11a, b, c and d: (a) the initial domain structure; (b) domain wall motion in a small field; (c) a change in domain arrangements and dominance of domains with particular magnetization directions in an intermediate field; and (d) a single domain and saturation of magnetization in a large field.

c) Concluding Remarks

Although the documentation of resultant crystal perfection with varying growth conditions has not been completed at this state, it can be concluded from the present results that in order to obtain highly perfect nickel crystals, I) bottlenecking at the initial stage of crystal growth is necessary, II) satisfactory diameter control is desirable during the entire period of growth, III) a polycrystalline or [111] oriented seed is preferable, in contrast with the previous results of copper single crystal growth,[2] and IV) there is a general trend towards a reproducible relationship between crystal perfection and growth conditions characterized by the practical process parameters describing the rotations of a seed and the melt. It is also worth mentioning that, when crystals are grown from a polycrystalline seed, the resultant growth direction usually turns out to be very close to [111]. This may explain why the results obtained from a polycrystalline seed are similar to those from a [111] seed. It has also been observed that the resultant crystal perfection is usually high, when boules are grown at a slower rate, say, .4 mm/min. This condition, however, creates some technical difficulty in routinely obtaining a bottleneck and controlling the diameter with our crystal growing apparatus.

As we have demonstrated, a proper choice of sets of process parameters is indeed require to improve crystal perfection to a certain level, as is the case for the copper crystal growth. The critical factor is, however, several crystallographic effects. For example, crystals with a spiral growth form can easily reach a certain level of perfection if the growth condition and the growth direction are

selected properly. The formations of Lomer-Cottrell dislocation locks and of curved small-angle grain boundaries all indicate that the ultimate level of crystal perfection is governed by some factors which diminish the generation of dislocations and make dislocations immobile. Anisotropic properties of crystals definitely make one direction more preferable than others. Even though the difference may be very small, it is significant for dislocations. An approach to the crystal growth mechanism through isotropic theories certainly is not adequate. It is indispensable to obtain knowledge on the behavior of dislocations in highly perfect crystals in order to accomplish the production of crystals free of dislocations.

It is also important to be aware of the fact that an initial crucial factor influencing the ultimate level of crystal perfection is found in the bottlenecking effect, or rather the original perfection in seed crystals. Purity of the melt should not be ignored; although we have not studied the effect of purity in this work, previous experiences with our metals have indicated that the purer the melt, the better the resultant perfection.

In this work, we have found that nickel single crystals like copper can be produced with the perfection far better ($\sim$400 dislocation lines/cm^2) than the existing level by controlling the practical process parameters and growth directions. Although they are not dislocation-free, the level of perfection is quite remarkable as a metal, and almost reaches the level which most semiconducting materials have so far enjoyed. These nickel crystals certainly serve as a precusor of commercial magnetic materials for the study of basic magnetic domain

properties under more idealized conditions.

Finally some comments will be made on crystal growth experiments in space, from our knowledge of ground based experiments on copper and nickel. Crystal growth experiments have no significant meaning, unless a careful choice of growth conditions are made and perfect seed crystals are used. Since most crystals can be made nearly perfect on earth if a careful and systematic study is made on the growth conditions, the lack of sensitive techniques for the characterization of crystal perfection often causes an incapability of distinguishing subtle changes in crystals grown in space from those grown on earth. It is imperative to use a sensitive technique, such as asymmetric (double) crystal topography (ACT) and scanning double crystal diffractometer (SCAD), for reliable characterization of crystal imperfections in crystals grown in space and/or on earth.

References

1. M. Kuriyama, J. G. Early and H. E. Burdette, "Characterization of Thermal Convection and Crystal Perfection in Metals Grown from the Melt," NBS report 10873 (1972).
2. M. Kuriyama, W. J. Boettinger, H. E. Burdette and R. M. Eaton, "Crystal Perfection in Czochralski Growth," NBSIR 74-611, 3-21 (1974).
3. M. Kuriyama, J. G. Early and H. E. Burdette, "Fluid Flow Effects on Crystalline Perfection," Proc. of AIAA 12th Aerospace Sciences Meeting, Paper No. 74-204 (1974).
4. M. Kuriyama, J. G. Early and H. E. Burdette, "An Immobile Dislocation Arrangement in As-Grown Copper Single Crystals Observed by X-Ray Topography," J. Appl. Cryst. 7, 535-540 (1974).
5. W. J. Boettinger, H. E. Burdette and M. Kuriyama, "Application of Contrast Conditions to Dynamical Images of Immobile Dislocations," Phil. Mag. 34, 1-9 (1976).
6. C. Kittel, "Physical Theory of Ferromagnetic Domains," Rev. Mod. Phys. 21, 541-583 (1949).
7. M. Kuriyama, "Distortion Correction in Anomalous Absorption Coefficients," phys. stat. sol. 24, 743-748 (1967).
8. M. Kuriyama, "X-Ray Diffraction from a Crystal Containing Isolated Imperfections," Acta Cryst. A25, S204 and 682-693 (1969).
9. M. Kuriyama and T. Miyakawa, "Primary and Secondary Extinctions in the Dynamical Theory for an Imperfect Crystal," Acta Cryst. A26, 667-673 (1970).

19. B. Roessler, "Observations of Ferromagnetic Domains by Anomalous Transmission of X-Rays; The Effect of Variation in the Reflecting Plane," phys. stat. sol. 20, 713-723 (1967).

20. M. Kuriyama and G. M. McManus, "X-Ray Interference Fringes and Domain Arrangements in Fe+3 wt% Si Single Crystals," phys. stat. sol. 25, 667-677 (1968).

21. M. Polcarová and J. Gemperlová, "Distortion of an Fe-Si Single Crystal and X-Ray Topographic Contrast due to a 90° Ferromagnetic Domain Wall," phys. stat. sol. 32, 769-778 (1969).

22. M. Polcarová and A. R. Lang, "On the Fine Structure of X-Ray Topographic Images of 90° Ferromagnetic Domain Walls in Fe-Si," phys. stat. sol. (a) 4, 491-499 (1971).

23. C. Wu and B. Roessler, "X-Ray Topographic Observations of Dislocation Ferromagnetic Domain Interactions in Fe 3% Si Crystals," phys. stat. sol. (a) 8, 571-579 (1971).

24. M. Schlenker and M. Kleman, "X-Ray Topographic Investigations of Ferromagnetic Domain Structures with Closure Domain Configurations in Iron-Silicon Single Crystals," J. de Phys. 32, C1-256 (1971).

25. S. Nagakura and Y. Chikaura, "X-Ray Topography of Magnetic Domains in Iron Whisker Crystals," J. Phys. Soc. Japan 30, 495-515 (1971).

26. M. Kuriyama, W. J. Boettinger and H. E. Burdette, "X-Ray Topographic Observation of Magnetic Domains in Czochralski-Grown Nickel Single Crystals in Anomalous Transmission Geometry," J. Appl. Phys. 47, 5064-5068 (1976).

27. M. Kuriyama, W. J. Boettinger and H. E. Burdette, "X-Ray Surface Reflection and Transmission Topography of Magnetic Domain Walls

10. M. Kuriyama, W. J. Boettinger and H. E. Burdette, "Crystal Perfection in Czochralski Growth," NBSIR 76-980, 3-21 (1976).

11. W. J. Boettinger, H. E. Burdette, M. Kuriyama and R. E. Green, Jr., "Asymmetric Crystal Topographic Camera," Rev. Sci. Instrum. 47, 18-23 (1976).

12. The trade name is included for completeness and does not represent a product endorsement.

13. R. W. Armstrong, W. J. Boettinger and M. Kuriyama, "Subgrain Misorientations in Melt-Grown Nickel Crystals via ACT," to be published.

14. Y. Chikaura, H. Fukumori and S. Nagakura, "Growth and Structure of Nickel Plate Crystals from Nickel Bromide by Reduction," Japan. J. Phys. 11, 1582-1583 (1972).

15. V. Alex, L. V. Tikhonov and O. Brümmer, "Growth, Preparation and X-Ray Topography of Nickel Crystals," Kristall u. Technik 9, 643-645 (1974).

16. M. Polcarová and A. R. Lang, "X-Ray Topographic Studies of Magnetic Domain Configurations and Movements," Appl. Phys. Letters 1, 13-15 (1962).

17. B. Roessler, J. J. Kramer and M. Kuriyama, "Anomalous Transmission of X-Rays in Fe-3 pct Si Crystals and the Observation of Ferromagnetic Domains," phys. stat. sol. 11, 117-120 (1965).

18. M. Polcarová and J. Kaczer, "X-Ray Diffraction Contrast on Ferromagnetic Domain Walls in Fe-Si Crystals," phys. stat. sol. 21, 635-642 (1967).

in Czochralski-Grown Nickel Single Crystals," J. Mater. Sci., in print (1977).

28. M. Kuriyama, W. J. Boettinger and H. E. Burdette, "Crystal Perfections and Magnetic Domain Walls in Thick Czochralski-Grown Nickel Single Crystals" in Advances in X-Ray Analysis, Vol. 20 (1977).

29. W. J. Boettinger, H. E. Burdette, E. N. Farabaugh and M. Kuriyama, "Some Topographic Observations of the Effects of Dynamical Diffraction in Imperfect Metal Crystals," in Advances in X-Ray Analysis, Vol. 20 (1977).

Table I. Crystal Growth and Diffraction Conditions

Crystal Slice Number	Rotation Speed (RPM)			Pulling Speed (mm/min)	Seed Orientation	Remarks	Thickness L(mm)	ACT		Rocking Curve Width (FWHM)		μL (μ= 49.6 mm^{-1})
	Seed (X)	Crucible (Y)	Δ = X-Y					Surface	Transmission	220-Surface	111-Transmission	
120223	+10.34	+10.00	+0.34	1.0	Polycrystal	A,B		$(\bar{2}20)$ Multigrain	Unobtainable			
120224	+10.34	+10.00	+0.34	1.0	Polycrystal	A,B		Multigrain	Unobtainable			
120231	+10.34	+10.00	+0.34	1.0	Polycrystal	A,B		Multigrain	Unobtainable			
130221	+10.17	+10.00	+0.17	1.0	Polycrystal	B		$(\bar{2}20)$ Multigrain	Unobtainable			
140231	+10.44	+10.00	+0.44	1.0	Polycrystal	B	.85	$(\bar{2}20)$	$(11\bar{1})$; $(11\bar{1})$w/Fields	34.0 sec	13.0 sec	42.2
164225	+10.00	+ 9.68	+0.32	1.0	[100]	B		$(\bar{2}20)$	$(11\bar{1})$ A few grains			
170231	+10.00	+ 9.75	+0.24	1.0	Polycrystal	B	.60	$(\bar{2}20)$	$(11\bar{1})$	30.4 sec	10.4 sec	29.8
170241	+10.00	+ 9.75	+0.24	1.0	Polycrystal	B	.45	$(\bar{2}20)$; $(2\bar{2}0)$	$(11\bar{1})$; (111); $(1\bar{1}1)$ (220); $(00\bar{2})$; Tilts All flipped	36.6 sec	10.5 sec	22.4
180231	+10.17	+10.00	+0.17	1.0	Polycrystal	B	.37	$(\bar{2}20)$; (220)w/Fields	$(1\bar{1}1)$; $(1\bar{1}\bar{1})$w/Tilt $(11\bar{1})$; $(1\bar{1}\bar{1})$Flipped	26.9 sec	12.6 sec 29.8 sec for (220)	18.5
180232	+10.17	+10.00	+0.17	1.0	Polycrystal	B	.57	$(\bar{2}20)$	$(1\bar{1}\bar{1})$	30.8 sec	12.1 sec	28.1
180241	+10.17	+10.00	+0.17	1.0	Polycrystal	B		$(\bar{2}20)$	$(11\bar{1})$			
180241A								$(\bar{2}20)$	(111)			
194231	+10.34	+ 9.83	+0.51	1.0	[100]	A,B		$(\bar{2}20)$	(002)			
194241	+10.34	+ 9.83	+0.51	1.0	[100]	A,B		$(\bar{2}20)$	Unobtainable			
234231	+10.00	+ 9.68	+0.32	1.0	[100]	B		$(\bar{2}20)$	Very faint			
234241	+10.00	+ 9.68	+0.32	1.0	[100]	B		$(\bar{2}20)$	Unobtainable			
244231	+10.00	+ 9.68	+0.32	1.0	[100]	B		Multigrain	Unobtainable			
244232	+10.00	+ 9.68	+0.32	1.0	[100]	B		Multigrain	Unobtainable			
274231	+10.34	+10.00	+0.34	1.0	[100]	C		$(\bar{2}20)$ Multigrain	Unobtainable			
280231	+10.07	+ 9.93	+0.14	.4	Polycrystal			$(\bar{2}20)$	(111)			
280232	+10.07	+ 9.93	+0.14	.4	Polycrystal		.55	$(\bar{2}20)$	$(11\bar{1})$; $(11\bar{1})$w/Field	30.8 sec	12.5 sec	27.4
292231	+10.34	+10.06	+0.28	.4	[110]			$(\bar{2}20)$ Multigrain	Unobtainable			
310231	+10.00	+10.20	+0.20	.4	Polycrystal			$(\bar{2}20)$	(111)			
310232	+10.00	+10.20	+0.20	.4	Polycrystal		.73	$(\bar{2}20)$	$(11\bar{1})$; (111) $(11\bar{1})$w/Field	36.0 sec	8.0 sec	36.0
333231	+10.03	+10.12	-0.08	1.0	[111]		.63	$(\bar{2}20)$	$(11\bar{1})$; (220)	33.0 sec	10.0 sec	31.4
333232	+10.03	+10.12	-0.08	1.0	[111]		.66	$(\bar{2}20)$	$(11\bar{1})$	26.0 sec	9.5 sec	32.6
344232	+10.14	+10.00	+0.14	1.0	[100]	C		Multigrain	Unobtainable			
352231	+10.17	+ 9.98	+0.19	1.0	[110]	C		Multigrain	Unobtainable			
352232A								Multigrain	Unobtainable			
363232	+10.27	+10.00	+0.27	1.0	[111]	C	.41	$(\bar{2}20)$	$(11\bar{1})$	26.5 sec	11.5 sec	20.3
376232	+10.10	+ 9.87	+0.23	1.0	[111]*	C		$(\bar{2}20)$ Damaged				
380231	+10.35	+10.07	+0.28	1.0		C	.71			23.0 sec	8.5 sec	35.4
390632	+11.03	+ 8.90	+2.13	1.0			1.02	$(\bar{2}20)$	$(11\bar{1})$; $(11\bar{1})$w/Field	35.5 sec	10.8 sec	50.5
406531	+21.13	+17.44	+3.69	1.0			.58			24.0 sec	11.5 sec	29.0
416331	+20.17	+20.00	+0.17	1.0	[111]*	C		$(\bar{2}20)$	$(11\bar{1})$	25.5 sec	9.5 sec	
416332	+20.17	+20.00	+0.17	1.0	[111]*	C		$(\bar{2}20)$	(111)	39.0 sec	13.5 sec	
390631	+11.03	+ 8.90	+2.13	1.0	Polycrystal			$(\bar{2}20)$; $(2\bar{2}0)$	$(11\bar{1})$	25.5 sec	9.5 sec	
406532	+21.13	+17.44	+3.69	1.0	[111]*			$(\bar{2}20)$	(111)			
376231	+10.10	+ 9.87	+0.23	1.0	[111]*			Badly strained				
363231	+10.27	+10.00	+0.27	1.0	[111]*		.78	$(\bar{2}20)$	(111)	22.0 sec	10.6 sec	38.8

A = No bottleneck B = Poor diameter control C = Spiral growth * = [111] seed grown from original polycrystal seeds

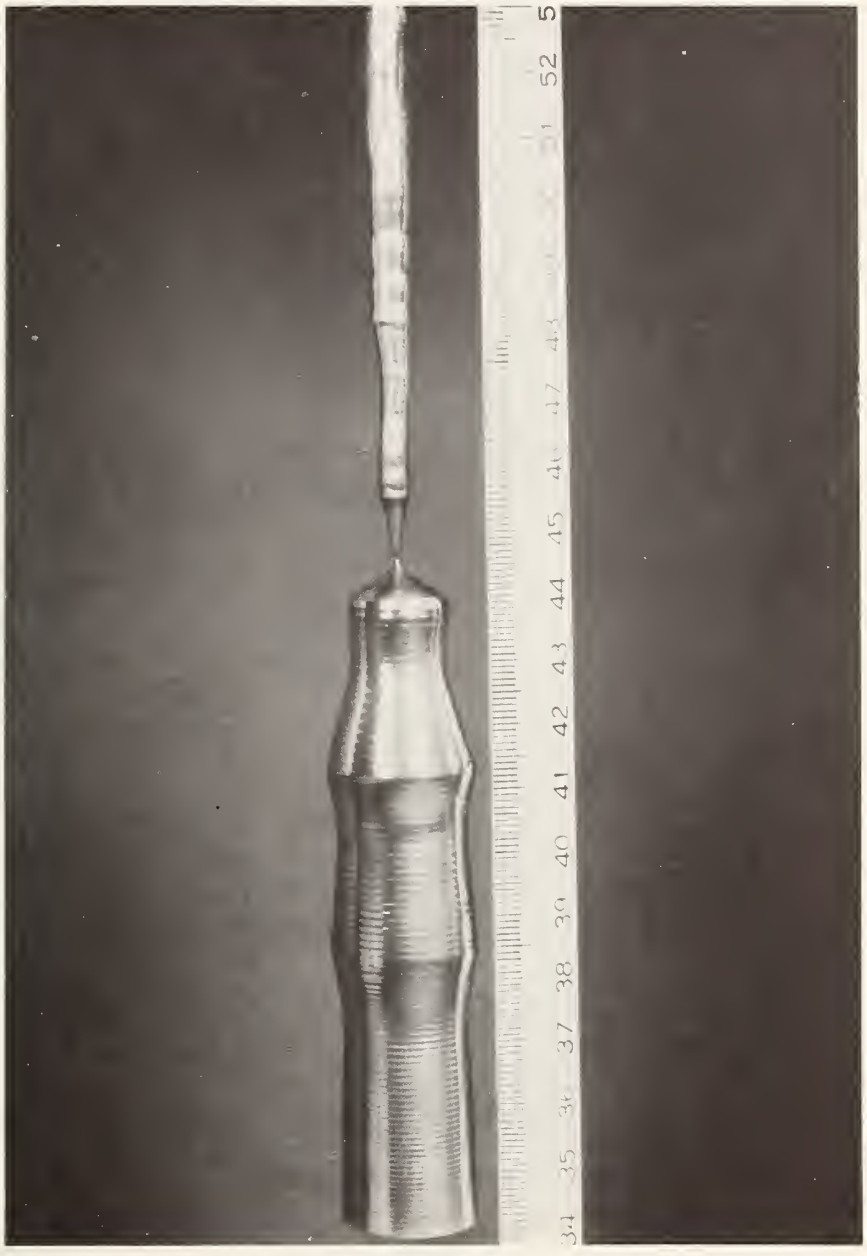

Fig. 1 Photograph of a Ni single crystal grown by the Czochralski technique with bottleneck diameter roughly 1 mm.

Fig. 2 Czochralski-grown Ni single crystal boule #274200 with spiral growth form. This shape is to be contrasted with the usual cylindrical growth form obtained by the Czochralski technique. Note also the small bottleneck which has been obtained near the seed material.

a

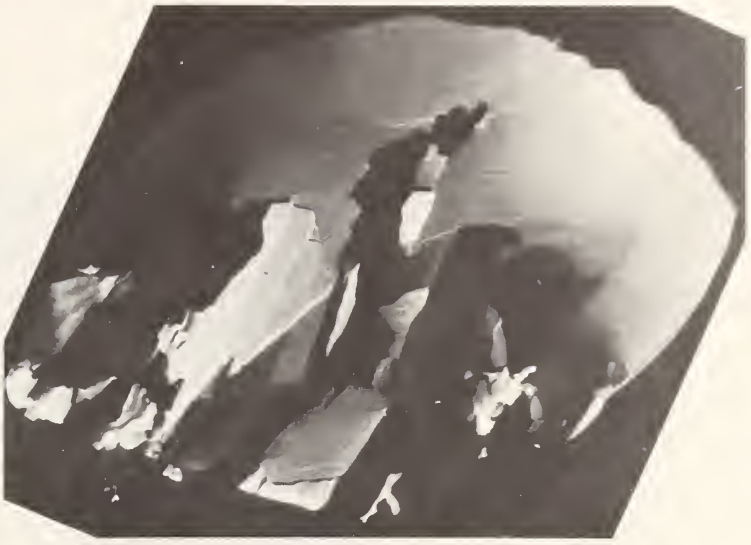

b

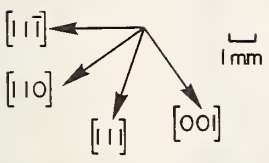

c

d

Fig. 3 ACT ($\bar{2}20$) surface reflection topographs of nickel crystals of increasing perfection; a) grown with a [110] seed; b) grown with a [100] seed, indicating misorientation of about 100 seconds of arc; c) grown with a [111] seed under poor diameter control, indicating misorientation of about 20 seconds of arc; d) grown with a [111] seed and good diameter control, indicating absence of subgrain structure.

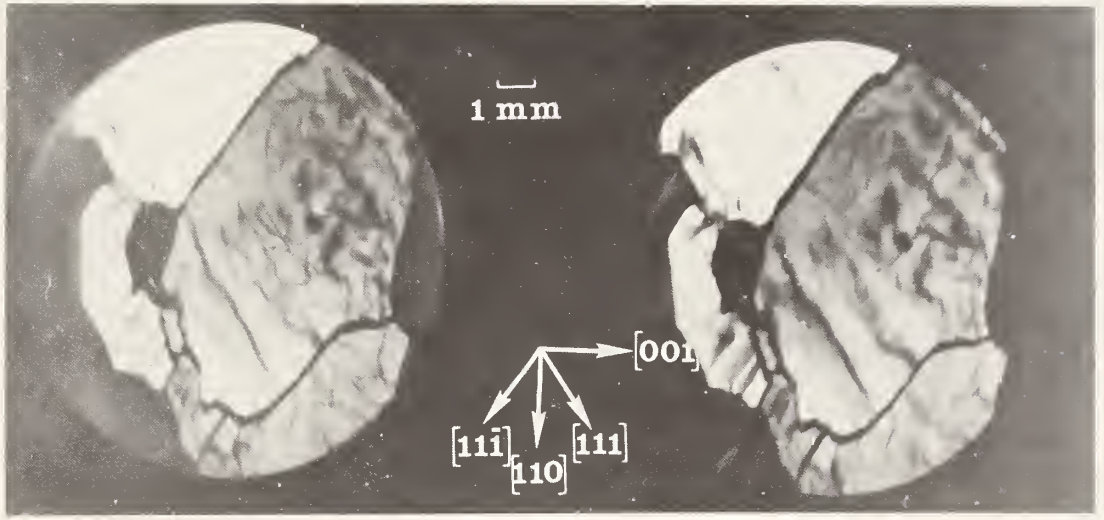

Fig. 4 ACT (200) transmission topographs of a) the 0-diffracted beam and b) the H-diffracted beam from a nickel crystal grown with a [100] seed without a bottleneck and without a good diameter control.

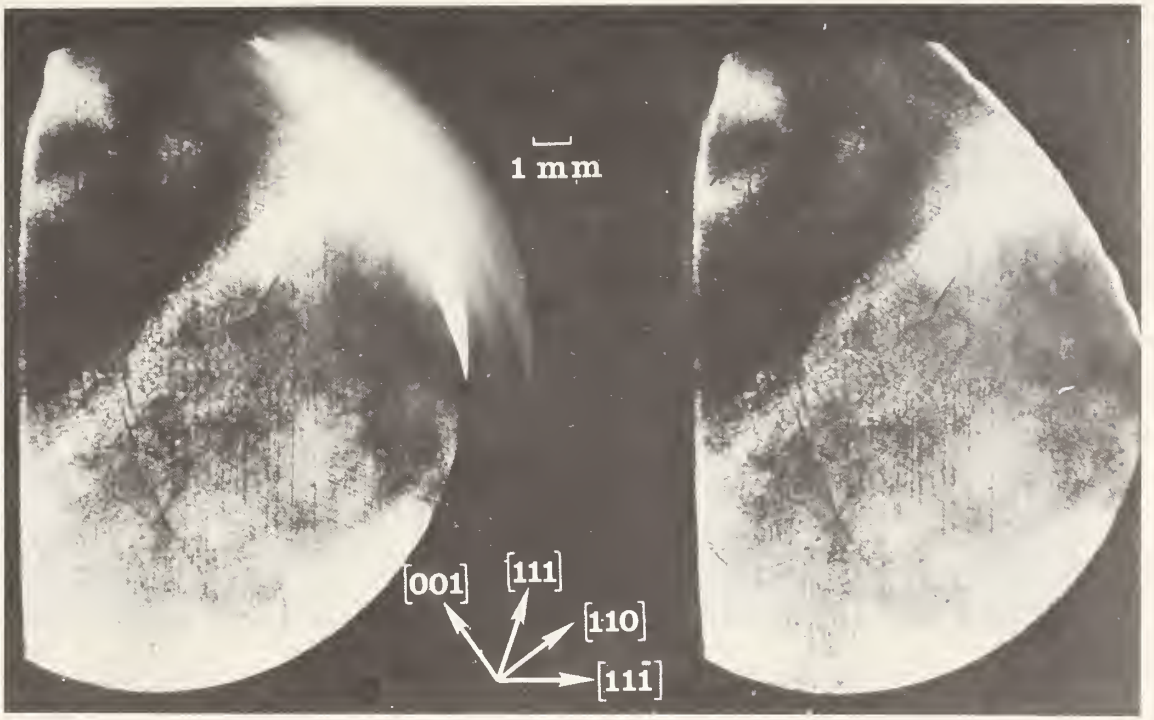

Fig. 5 ACT (11$\bar{1}$) transmission topographs of crystal #280232 showing an arrangement of Lomer-Cottrell sessil dislocations. (a) 0-diffracted beam; (b) H-diffracted beam.

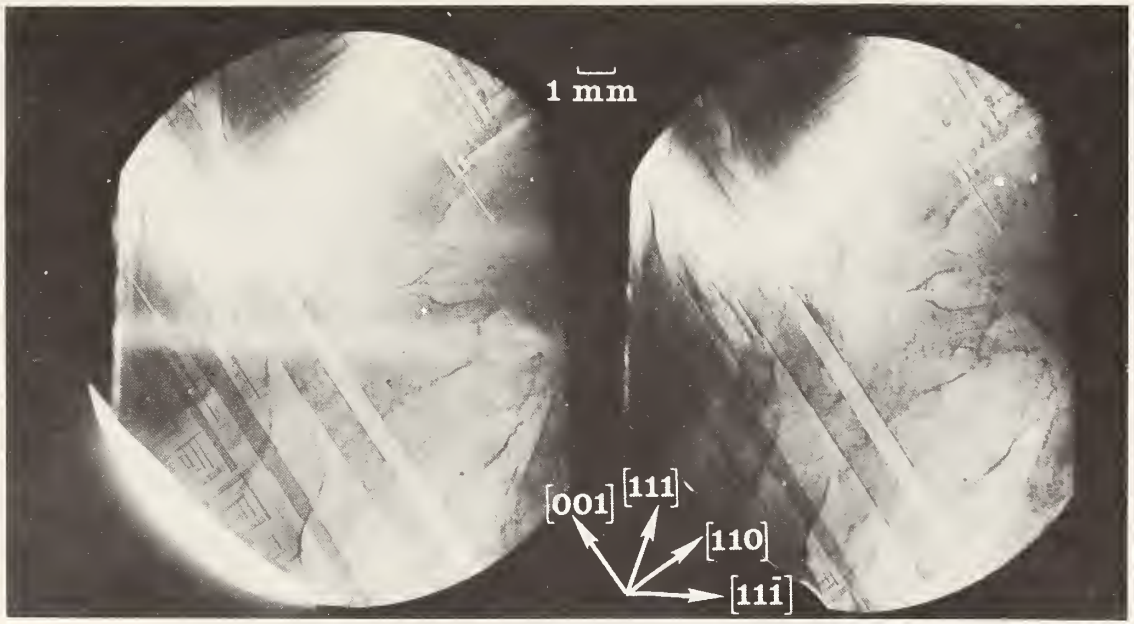

Fig. 6 ACT (11$\bar{1}$) transmission topographs of crystal #363232. (a) 0-diffracted beam; (b) H-diffracted beam. Very small angle grain boundaries are visible along with isolated dislocations and rectangular formations of magnetic domain walls.

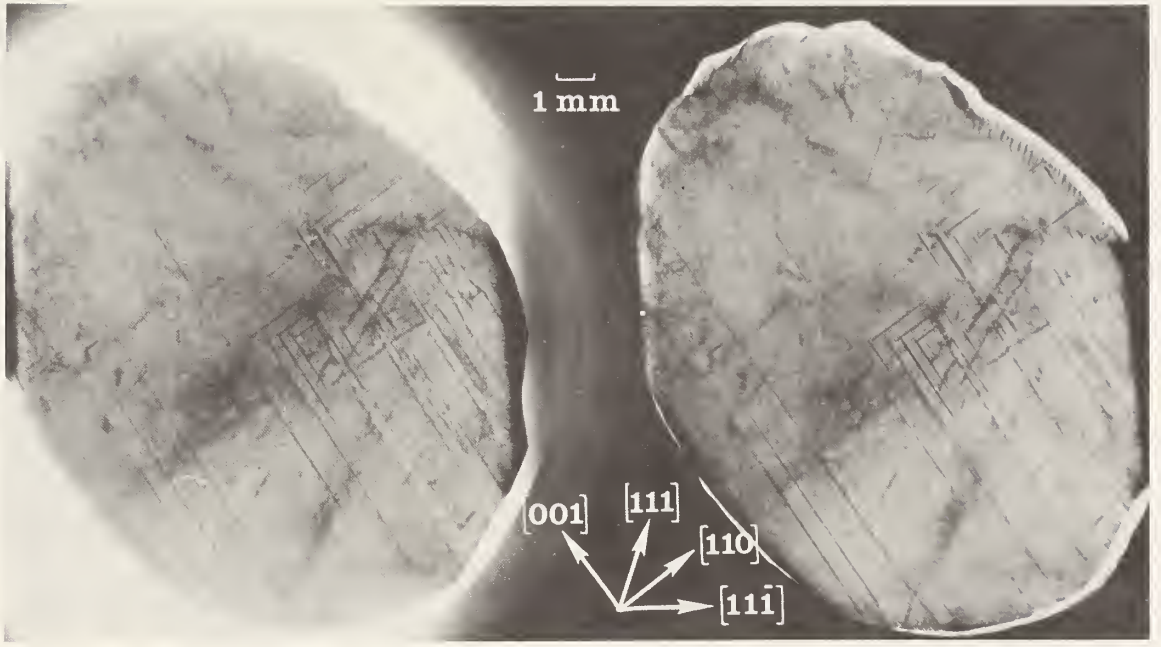

Fig. 7 ACT (11$\bar{1}$) transmission topographs of crystal #310232. (a) 0-diffracted beam; (b) H-diffracted beam. Isolated dislocation images are distinctly visible along with rectangular formations of magnetic domain walls.

Fig. 8 ACT ($\bar{2}20$) surface reflection topograph of nickel crystal showing subgrain boundaries some of which are parallel to <111> directions. The misorientation of these subgrains is about 300 sec.

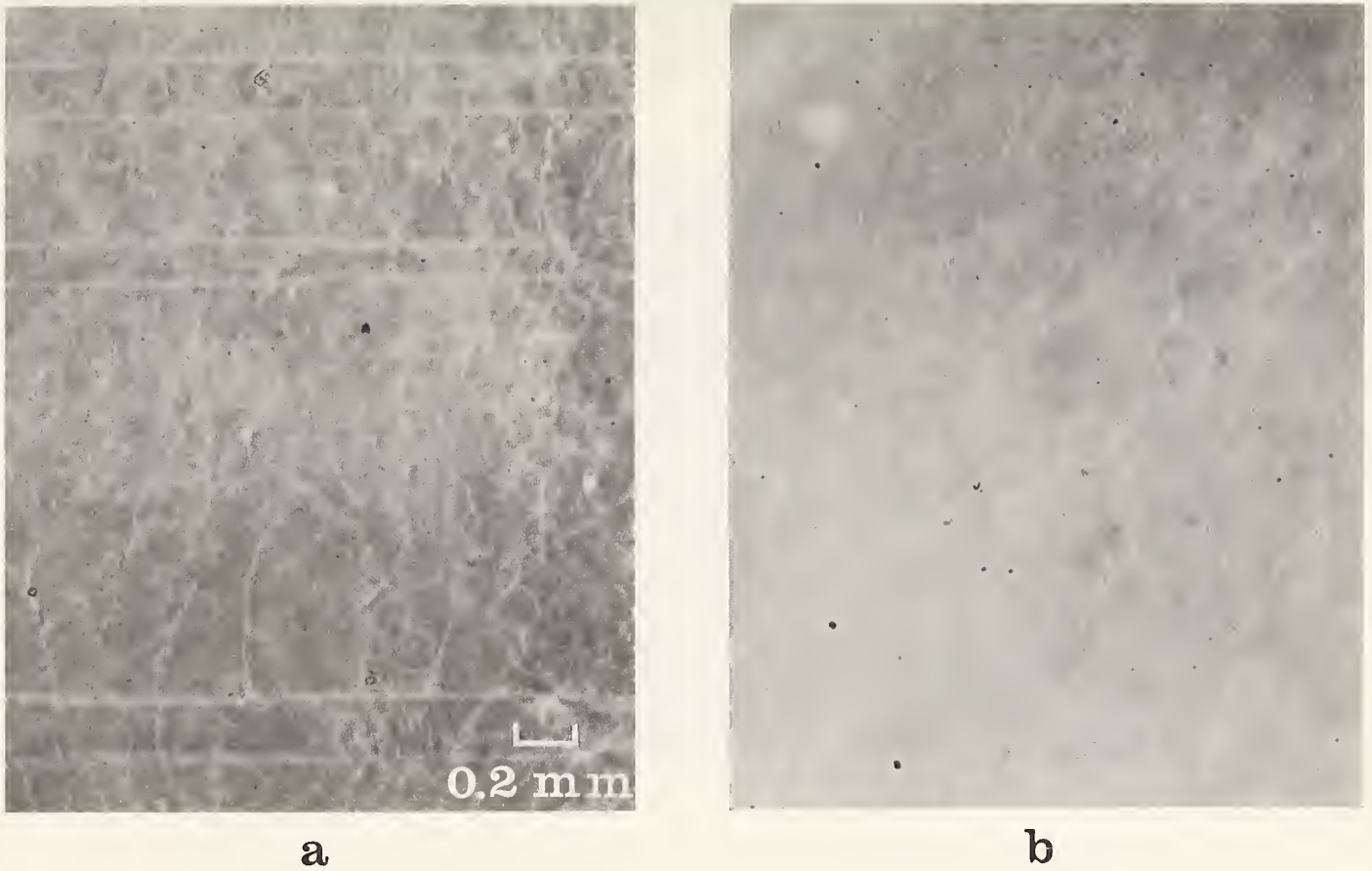

Fig. 9 ACT transmission topographs of different nickel crystals showing low dislocation densities of about 400 dislocation lines/cm^2 or less. a) a crystal 0.63 mm thick, b) a crystal 0.41 mm thick. The horizontal line images in (a) are magnetic domain walls.

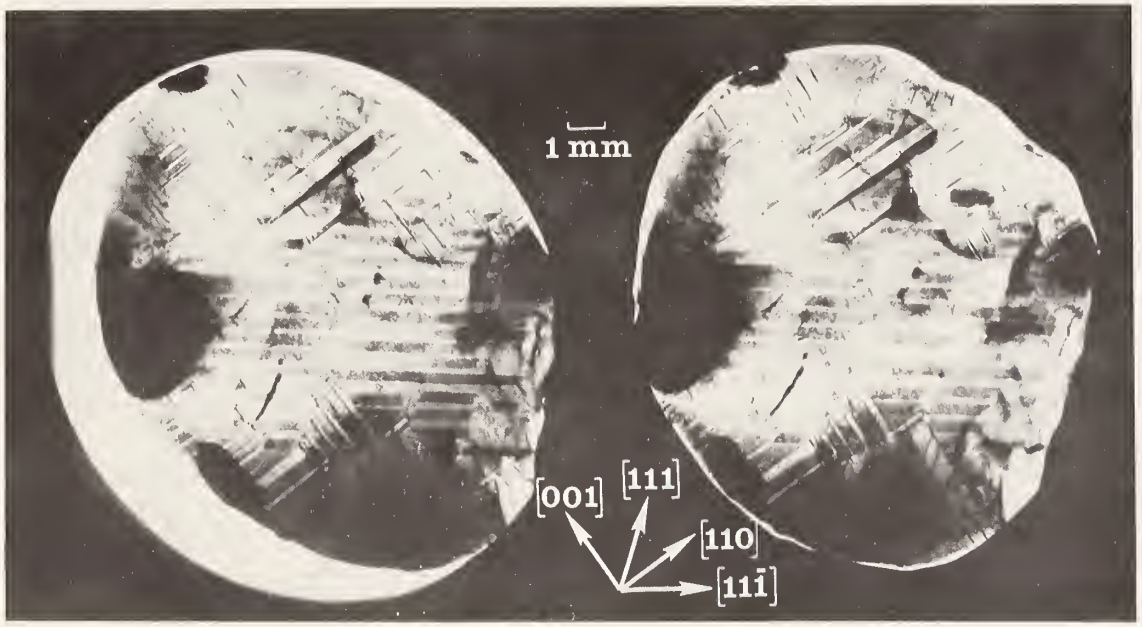

Fig. 10 ACT (11$\bar{1}$) transmission topographs of crystal #180231, showing oblique magnetic domain walls. (a) 0-diffracted beam; (b) H-diffracted beam.

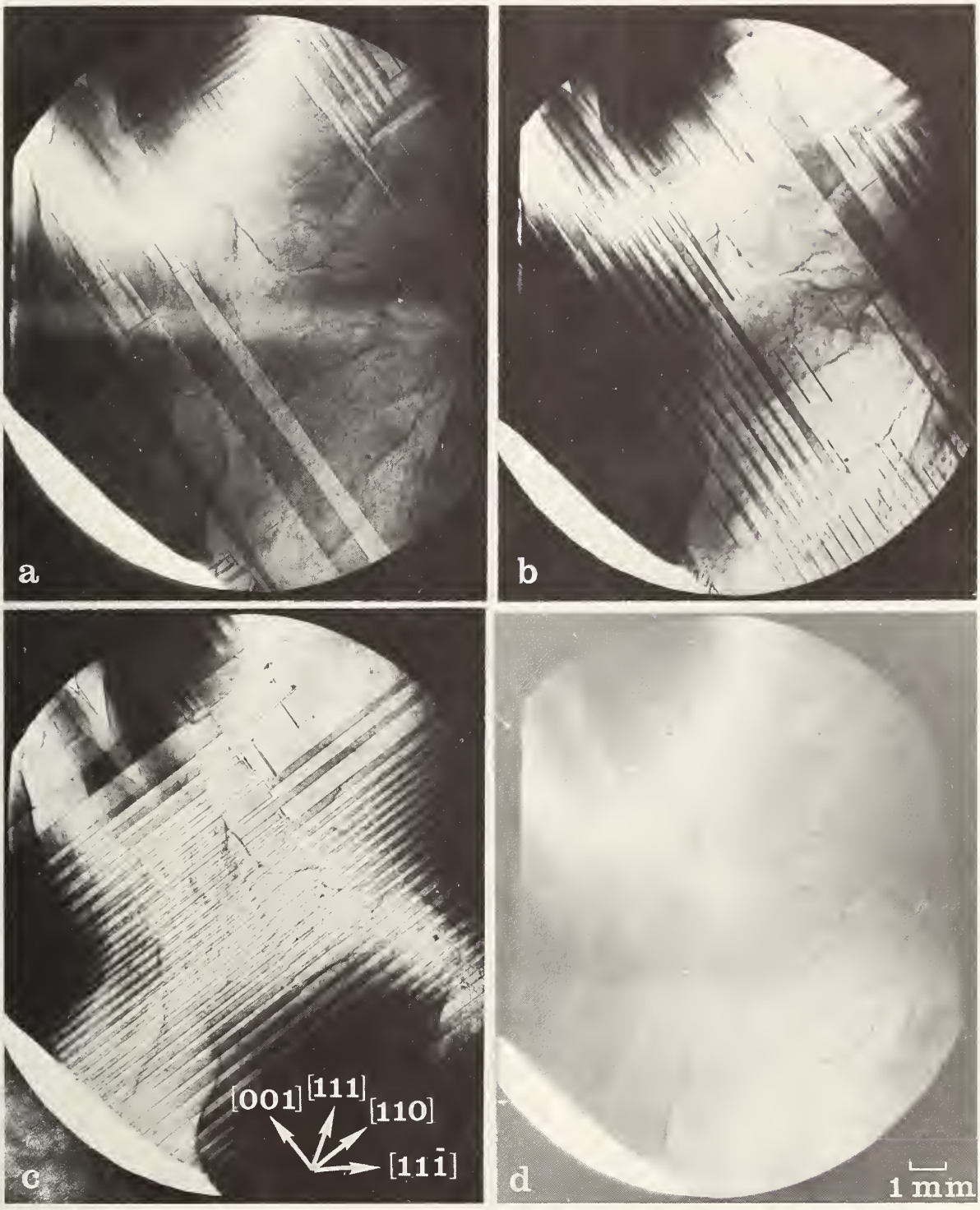

Fig. 11 ACT (11$\bar{1}$) transmission topographs of crystal #363232 showing changes in the domain structure as an external magnetic field is applied. (a) the initial domain structure; (b) domain wall motion in a small field; (c) a change in domain arrangement and dominance of domains with particular magnetization directions in an intermediate field; and (d) a single domain and saturation of magnetization in a large field.

Task 2

Evaporative Preparation of Ultrahigh Purity Materials
Part A: Mass Spectrometric Studies of Vaporization Processes

E. R. Plante

Inorganic Materials Division
Institute for Materials Research

Summary

Part A of task 2 has involved studies by mass spectrometry and optical pyrometry of the apparent vapor pressure and temperature of radiatively heated aluminium oxide supported as a sessile drop. Previous studies have shown that an apparent increase in the vapor pressure of a factor of 3 on melting is due to an actual increase in the temperature of the molten Al_2O_3 to a temperature well above the melting point. Although this effect had been observed prior to this work, it had erroneously been attributed in the literature as being due to a discontinuous increase in the vaporization coefficient at the melting point.

Experiments were undertaken during this contract period in an attempt to better control the temperature of the supported drop in the vicinity of the melting point by using more nearly isothermal furnaces. However, it did not prove possible to achieve stable sessile drops of alumina under more isothermal conditions and it was concluded that it would probably be more profitable to study the purification and/or evaporation behavior of materials by more conventional techniques such as the Knudsen effusion method. Future vaporization studies associated with thermochemical studies of corrosive reactions in oxide

materials will be made using this method under a continuing NASA contract. Problems related to temperature measurement of levitated melts in tube furnaces for space experiments are briefly mentioned.

Part A: Mass Spectrometric Studies of Vaporization Processes

Introduction

The objective of part A of task 2 has been to study the vaporization characteristics of non-conducting liquids under conditions resembling those which might be encountered in high temperature space processing. Although the major interest was initially on purification processes, it became evident during the program that problems involving temperature control and measurement of radiatively heated non-conductors supported as sessile drops were of greater importance to earth bound experiments and might be of considerable importance to space processing experiments. These problems in temperature control and measurement can become important in cases where a material is heated in a non-uniform radiation field, the energy transfer is largely by radiation, and where discontinuous changes in emissive properties occur at a melting point. The principal effort during the past year has involved attempts to better control these effects in order to observe vaporization behavior of liquid Al_2O_3 under container free conditions.

Experimental Procedures

The experimental procedures and previous results have been reported in detail (1,2). Briefly, commercially available Al_2O_3 rods were mounted in the sampling position of a modulated beam, mass spectrometric system and observed by optical pyrometry and mass spectrometry when the tip of the alumina rod was heated and became molten. Heating was accomplished by radiation transfer between a resistively heated tungsten furnace and the alumina rod. Since the mass spectrometer is highly

evacuated with background pressure of the order of 1×10^{-7} torr, free vacuum evaporation conditions are achieved. Under these conditions it was observed that when the Al_2O_3 sample melted an increase in the apparent vapor pressure of approximately a factor of 3 and a decrease in apparent temperature of several hundred degrees took place. Although this phenomena had been observed and described in the literature previously (3), it had been attributed to a discontinuous increase in the vaporization coefficient of alumina at the melting point.

A second type of experiment in which Al_2O_3 was melted in a shallow container so that free evaporation conditions would be maintained but a significant fraction of the energy transfer was by conduction, did not show an increase in the pressure on melting although a decrease in apparent temperature was observed. Since the vapor pressure is a fundamental property of a material it was concluded that in the sessile drop experiments an actual increase in the temperature or T-jump had taken place when the sample melted. It was possible to account for the general behavior observed in the sessile drop experiment by the changes in the total and spectral emissivities of solid and molten alumina and the conductivity loss of the alumina sample due to its support, by balancing the radiation gains and losses at the melting point when the alumina was solid and when it was molten. The apparent decrease in temperature on melting can be accounted for by the decrease in reflectivity of molten alumina as compared to solid alumina and the non-ideal nature of the heater and sample arrangement which results in the heater being much hotter than the sample.

Experimental Results

Experimental work during the past year has been carried out with two objectives in mind. First, the sessile drop arrangement was considered desirable because it simulates a condition which can be achieved in space research; namely, that there is no physical contact between a heated sample and a container. It is recognized however that interaction of the sample and its environment *via* gas-solid reactions is possible. Secondly, it was considered worthwhile to attempt such experiments under conditions in which more uniform heating was achieved.

In principle, the use of a more ideal furnace-sample arrangement would; (a) decrease the magnitude of the temperature measurement error caused by reflection or radiation from the sample surface, (b) decrease the magnitude of the T-jump caused by an increase in the total emissivity of the sample on melting and, (c) would lead to more accurate temperature measurement both above and below the melting point. Balanced against these objectives however is the requirement that the production of a stable sessile drop requires the presence of a temperature gradient at the droplet-solid interface. Thus, only an approach to ideal isothermal conditions can be achieved. In addition, the sessile drop owes its stability to the surface tension of the liquid and since the surface tension usually decreases with increasing temperature, the temperature range of a stable sessile drop will be limited.

Attempts at achieving these objectives were for the most part negative. It appears that sessile drops of relatively pure Al_2O_3 are quite fluid and difficult to support in vacuum. Relatively large sessile drops of tantalum oxide-contaminated Al_2O_3 could be supported

but these were not considered worthy of further experimentation.

Other measurements were made using relatively open tungsten heaters in which an attempt to reduce the magnitude of the T-jump was made by using longer heaters which have the effect of reducing thermal conductivity losses. The results of these experiments however did not differ appreciably from those in which short conical heaters were used to heat the sample. With the sample somewhat below the melting point, an apparent temperature of 2030°C (uncorrected for window, prism,and modulation disk) was observed while on melting the apparent temperature would typically decrease to 1920°C. In the molten state an image of the heater was apparent on the sample surface and appeared as alternating light and dark regions on the sample surface. This indicated that a molten alumina surface has a high degree of specular reflection.

Conclusion and Discussion

The results of this part of task 2 suggests that the use of sessile drop as a means of support for molten liquids places severe restrictions on the type and validity of the data that can be obtained. The observations of T-jump, and pressure discontinuity are real observable effects but they result from very strong interactions between the experimental apparatus and the sample. Thus, they are not properties of the sample alone. The results of these experiments indicate that it would be more profitable to study the purification and/or evaporation behavior of materials by more conventional techniques such as the Knudsen effusion method and try to determine if important interaction problems are encountered between the sample and its container. Studies of this method are planned for a continuing NASA project.

Some of the results of this work lead to questions concerning whether or not similar temperature measurement problems or temperature discontinuity effects encountered in space experiments involving levitated melts of materials heated in tube furnaces in cases where energy transfer is mainly by radiation. The extent to which this type of effect can occur depends among other things on the relative sizes of the sample and furnace cavity as well as on the temperature distribution of the furnace and the emissive properties of the sample. This problem may become apparent if the temperature homogeneity of the furnace is compromised in order to provide positioning devices and observation ports. Because of the complexity of this problem it will probably have to be dealt with on an ad hoc basis.

References

[1] Passaglia, E., and Parker, R. L., NBS Space Processing Research, NBSIR 76-980, 25-39.

[2] Paule, R. C., Mass Spectrometric Studies of Al_2O_3 Vaporization Processes, High Temp. Sci., 8, 257 (1976).

[3] Burns, R. P., Jason, A. J., and Inghram, M. G., Discontinuity in the Rate of Evaporation of Aluminum Oxide, J. Chem. Phys., 40, 2739 (1964).

Task 2

Evaporative Preparation of Ultra-High Purity Materials

Part B. Evaporative Purification of Refractory Metals Using R.F. Levitation

W. J. Boettinger and F. S. Biancaniello

Metallurgy Division
Institute for Materials Research

Summary

To obtain quantitative data on the rate of purification of refractory alloy melts under well-characterized conditions, samples of Mo and Nb have been R.F. levitation melted, held liquid for times up to 30 min. and frozen in vacuum without a container. By initial and final chemical analysis of selected impurities, rates of purification of the samples are obtained and compared to calculations of such evaporations. Advantages of R.F. levitation for this purpose are rapid heating to and cooling from test temperature, excellent stirring in the liquid to prevent transport limitation in the liquid, and an isothermal and simply shaped evaporation surface.

In this work rates of purification are determined for Nb-2 w/o Mo and Nb-5 w/o Mo at 2900K and for Mo-1 w/o Zr and Mo-5 w/o Zr at 3000K. These rates of purification agree quite well with predictions of calculations based on Knudsen evaporation of a well-stirred isothermal ideal binary solution of the two components.

Introduction

The continuing search for new materials with new or improved properties requires simultaneous advances in techniques of material

preparation and processing. One such possible advance is the ability present in microgravity to process substantial quantities of high temperature materials without a container in vacuum. Regardless of the particular material involved in such a process, the evaporation of volatile constituents will have an important role.

This work has been performed to determine the ability of calculations to correctly predict the rate of purification of materials by the evaporation of volatile impurities. In a previous report,[1] methods for the calculation of the purification rate of materials where complex interactions between vapor species are present have been formulated. These calculations are necessary to handle, for example, the purification of CaO from Al_2O_3. In order to provide an overall check of the calculation under more simple conditions, however, the measurement of purification rate of several simple binary liquid alloys has been undertaken here. These measurements are made under the well-defined experimental conditions available through the use of the technique of R.F. levitation melting in vacuum. This report will conclude the work on this subject and hence a brief summary of prior accomplishments will be made.

Previously, the development of a R.F. levitation system was described[2,3] which accomplished the melting, holding at test temperature and solidification of small (3-4g) metal samples in vacuum without a container in the temperature range of 2600-3100K. The routine accomplishment of solidification during levitation without the introduction of a quenching gas is unique to this task. Also the ultra-purification

of Fe from Mo has been accomplished[3]. Samples initially containing 50 ppm Fe were purified to less than 50 ppb in approximately six seconds. A major conclusion drawn here was that the transport of impurities to the evaporation surface was very rapid and that the assumption of a completely-stirred sample was accurate for R.F. levitated samples.

The work reported herein, consists of measurements of the purification rate of Mo and Nb with the intentionally added impurities of Zr and Mo respectively at levels of 1 to 5 w/o. These impurities give purification rates sufficiently slow to permit meaningful analysis of data. The rather high levels of impurity were employed to permit greater accuracy in the chemical analysis of samples. These results are compared to calculated rates of purification which were developed previously[3]. For Nb-Mo alloys the calculation agrees with the experimentally determined values within the experimental error. For the Mo-Zr alloys the agreement is good, but a slight discrepancy is attributed to possible deviation from ideal solution behavior.

Experimental Procedures

The R.F. levitation apparatus has been described in detail previously,[2,3] but a brief description will be given here. Samples (3-4g) are placed in a R.F. coil consisting of two identical opposing conical sections of three turns each with a base diameter of approximately 2 cm. After evacuation of the vacuum chamber to less than 7×10^{-5} Pa, the coil is energized causing the sample to be levitated and to be quickly melted. The sample is then brought to the desired test temperature. After a predetermined time, the sample is frozen and cooled to

about 200K below the solidus temperature while still levitated in vacuum. The sample is then dropped into a copper dish. Temperatures are measured using an automatic optical pyrometer which sights through a moving window to prevent errors due to vapor condensation. Absorbtion by the window and emissivity of the sample are accounted for by measuring the apparent melting temperature of pure Mo or Nb. Temperature measurements are considered to be accurate to about 15K.

After cooling to room temperature, samples are removed from the vacuum and cut and etched for chemical analysis. Half of the sample is analyzed to minimize the effects of solute segregation which may occur upon solidification. Samples were analyzed by the Analytical Chemistry Division of NBS by Atomic Absorption Spectrometry or by Flame Emission Spectrometry. (See Appendix.) For Nb-Mo and for Mo-Zr, values are considered to be accurate to about 2% and 4% respectively of the values stated.

Preparation of samples for levitation required considerable care. Because fairly high impurity levels (1-5 w/o) were required to simplify chemical analysis, impurities must be artificially introduced into metal samples. Alloys have been prepared by powder metallurgy and by inert gas arc-melting. In the former, samples were pressed from elemental powders and sintered at 1700K in vacuum. Although this procedure produces samples which can be levitation melted, the oxygen content of these samples is quite high (0.5 w/o). Such high oxygen contents will effect the evaporation rate of Zr and complicate the results of purification experiments. This necessitated the use of the alternative method of sample preparation. Four alloy ingots of approximately 60g with

nominal composition Mo-1 w/o Zr, Mo-5 w/o Zr, Nb-2 w/o Mo and Nb-5 w/o Mo were prepared by arc-melting on a cold copper hearth under gettered argon. This produced Mo-Zr alloys with less than 100 ppm O. Ingots were remelted several times to maximize homogeneity. These ingots were cut into approximately 4g samples for levitation. Several smaller samples from different parts of each ingot were retained for chemical analysis to represent the initial composition of the samples taken from each ingot. The values obtained from these samples are given in Table I along with the mean values. In addition to the alloy samples, pure Nb and Mo samples were also levitated and held molten for various lengths of time to determine the vapor pressure of the pure base metals. These experiments were performed in an identical manner with the experiments for the metal with alloying addition. The Mo and Mo-based samples were purified at 3000K and the Nb and Nb-based samples were purified at 2900K. This represents about equal superheat for each. Although R.F. levitation permits extremely rapid heating to and cooling from test temperature, the sample is above $0.9T_m$ for about 1 minute longer than it is at test temperature. The effective time of evaporation is then slightly longer than the time at test temperature. However, the effect of this is small compared with the scatter in the results.

Experimental Results

The results of experiments on pure Nb, Nb-2.04 w/o Mo and Nb-5.02 w/o Mo are summarized in the first six columns of Table II. The last three columns will be described later. The experimental results are also shown in Figs. 1 and 2 where the composition as a function of time

TABLE I - Initial Composition

Nominal Composition	Composition (^{W}/o)	Mean (^{W}/o)
Nb-2^{W}/o Mo	1.92, 1.99, 2.04, 2.06, 2.09, 2.09, 2.11	2.04
Nb-5^{W}/o Mo	4.99, 5.01, 5.02, 5.03, 5.05	5.02
Mo-1^{W}/o Zr	0.98, 0.99, 1.00	0.99
Mo-5^{W}/o Zr	5.03, 5.08, 5.29, 5.37, 5.42	5.24

TABLE II - Summary of Experiments on Nb and Nb-Mo Alloys at 2900 K

	#	Initial Mass (g)	Final Mass (g)	Initial Composition (Mass Fraction Mo)	Final Composition (Mass Fraction Mo)	Time At Temperature (s)	α	$P_A \times 10^6$ (atm)	$P_B \times 10^5$ (atm)
Nb	11-1-76	3.7886	3.7358			463		4.845	
	5-11-76	3.7720	3.7104			695		3.766	
	6-22-76	3.5482	3.4908			714		3.416	
	11-19-76	3.7894	3.7146			731		4.348	
	11-23-76	3.7789	3.6834			1068		3.800	
	6-21-76	3.7883	3.6711			1423		3.499	
	6-16-76	3.7850	3.6721			1433		3.348	
	12-8-76	3.7793	3.6282			1534		4.185	
Nb-2w/o Mo	11-18-76	3.6817	3.6339	0.0204	0.0191	345	0.149	5.293	3.610
	11-9-76	3.7718	3.7180	0.0204	0.0192	360	0.175	5.797	3.366
	11-15-76	3.7510	3.6977	0.0204	0.0192	474	0.175	4.376	2.541
	11-8-76	3.7391	3.6614	0.0204	0.0186	702	0.169	4.289	2.579
	11-2-76	3.7863	3.7095	0.0204	0.0180	713	0.124	4.032	3.304
	11-12-76	3.7618	3.6546	0.0204	0.0171	1068	0.124	3.755	3.077
	11-11-76	3.7656	3.6583	0.0204	0.0138	1069	0.053	3.280	6.289
	11-4-76	3.7520	3.6124	0.0204	0.0157	1346	0.111	3.866	3.539
	11-5-76	3.7746	3.6338	0.0204	0.0159	1363	0.116	3.845	3.368
	11-16-76	3.7767	3.5995	0.0204	0.0154	1785	0.131	3.784	2.935
	11-17-76	3.7581	3.5849	0.0204	0.0149	1790	0.115	3.619	3.198
Nb-5w/o Mo	5-13-76	3.7885	3.7448	0.0502	0.0452	348	0.055	2.943	5.437
	5-14-76	3.7788	3.7307	0.0502	0.0485	350	0.233	5.012	2.186
	5-17-76	3.7225	3.6786	0.0502	0.0468	352	0.101	3.693	3.716
	5-18-76	3.7231	3.6762	0.0502	0.0473	355	0.133	4.245	3.243
	5-12-76	3.7844	3.6988	0.0502	0.0454	702	0.145	4.045	2.835
	5-10-76	3.7602	3.6758	0.0502	0.0418	707	0.068	3.122	4.666
	5-11-76	3.7688	3.6783	0.0502	0.0459	714	0.174	4.383	2.560
	5-21-76	3.7920	3.6349	0.0502	0.0407	1434	0.128	3.545	2.814
	5-26-76	3.7866	3.6305	0.0502	0.0410	1437	0.133	3.561	2.721

at test temperature is plotted respectively for the 2.04 w/o Mo and the 5.02 w/o Mo series.

The results of experiments on pure Mo, Mo-0.99 w/o Zr and Mo-5.24 w/o Zr are summarized in Table III. The composition versus time is plotted in Figs. 3 and 4 respectively for the 0.99 w/o Mo and 5.24 w/o Zr series.

Conclusions and Discussion

This section will first review the calculation of purification rate presented previously[3] and using available thermochemical data, show the relation between the experimental data and the calculated results. The small discrepancy between the two will then be examined in detail and information on the thermochemical data; specifically, the possible deviation from ideality of dilute liquid Mo-Zr and Nb-Mo alloys will be described.

a) Purification Rate

In a previous report,[1] calculations for the purification of materials where complex interactions between species are present has been performed. This computer program can be used (in a trivial fashion) to predict the rate of evaporation into vacuum of a well-stirred isothermal ideal binary solution of two metals. However, in this simple case the rate can be obtained analytically.

Let $n_A(t)$ and $n_B(t)$ be the number of moles of A and B present in the liquid at time t. Assuming Knudsen evaluation conditions apply, the relevant equations describing the purification process are:

TABLE III - Summary of Experiments on Mo and Mo-Zr Alloys at 3000 K

	#	Initial Mass (g)	Final Mass (g)	Initial Composition (Mass Fraction Zr)	Final Composition (Mass Fraction Zr)	Time At Temperature (s)	α	$P_A x 10^5$ (atm)	$P_A x 10^4$ (atm)
Mo	3-19-76	4.2638	2.9077			709		8.478	
	3-18-76	4.2484	2.6860			710		9.784	
	3-22-76	4.2528	2.8606			720		8.572	
Mo-1W/oZr	2-6-76	3.9535	3.4381	0.0099	0.0081	238	0.405	9.478	2.282
	2-23-76	4.2273	3.2888	0.0099	0.0068	497	0.396	8.281	2.039
	2-18-76	4.2558	2.7428	0.0099	0.0069	708	0.545	9.412	1.684
	2-20-76	4.2322	2.8579	0.0099	0.0056	722	0.403	8.340	2.018
Mo-5W/o Zr	3-8-76	4.2115	3.2711	0.0524	0.0411	400	0.486	9.958	1.998
	3-1-76	4.2424	3.3142	0.0524	0.0385	407	0.419	9.544	2.221
	3-11-76	4.2395	3.2709	0.0524	0.0389	414	0.440	9.828	2.178
	3-2-76	4.2503	2.7529	0.0524	0.0363	703	0.521	9.094	1.702
	3-12-76	4.2346	2.7127	0.0524	0.0365	710	0.531	9.160	1.682
	3-4-76	4.2272	2.7041	0.0524	0.0338	715	0.483	9.055	1.828
	3-3-76	4.2485	2.7201	0.0524	0.0357	720	0.516	9.054	1.711

$$P_A \frac{n_A}{n_A + n_B} = -k_A \frac{dn_A}{dt} \tag{1}$$

$$P_B \frac{n_B}{n_A + n_B} = -k_B \frac{dn_B}{dt} \tag{2}$$

where $k_i = \frac{(2\pi RTm_i)^{1/2}}{A}$ and

P_i = vapor pressure of pure i at temperature T

m_i = molecular weight of component i

A = area of sample available for evaporation

R = universal gas constant

T = absolute temperature.

The solution* when A is a constant is given by

$$\frac{n_A}{N_A} = \left(\frac{n_B}{N_B}\right)^{\alpha} \tag{3}$$

$$t = \frac{k_B N_A}{P_B} \left\{ \frac{N_B}{N_A} \left(1 - \frac{n_B}{N_B}\right) - \frac{1}{\alpha} \left[\left(\frac{n_B}{N_B}\right)^{\alpha} - 1 \right] \right\} \tag{4}$$

where N_A and N_B are the initial number of moles of A and B respectively and $\alpha = (p_A/p_B)\ (m_B/m_A)^{1/2}$.

*Equation (3) is valid even if A is not constant and even if there are other components in the solution.

It should be noted here that if the solution is non-ideal, this non-ideality can be treated for dilute solutions of component B and A by replacing p_B by $k_{H,B}$, the Henry's Law constant for B in A. It is well known that for dilute solutions which deviate from ideality, Henry's Law is obeyed for the solute and Raoult's Law is obeyed for the solvent[4]. In this case, the solution to Eqns. 1 and 2 is still given by Eqns. 3 and 4 with $k_{H,B}$ substituted for p_B. In the rest of this report, component A will be taken to be the solvent and component B, the solute, for any given alloy.

The parameters needed for the calculations are p_A, p_B(or $k_{H,B}$), T and A. Having no information on $k_{H,B}$, p_A and p_B are obtained from the JANAF Thermochemical Tables[5]. For Mo-Zr at 3000K, $p_A = 1.002 \times 10^{-4}$ atm, $p_B = 1.556 \times 10^{-4}$ atm. For Nb-Mo at 2900K, $p_A = 3.890 \times 10^{-6}$ atm, $p_B = 4.395 \times 10^{-5}$ atm. The sample has been assumed to be spherical and of constant area. Treatment of cases where the area changes significantly during purification can be treated using the original calculation by Paule[1]. The densities of liquid Mo and liquid Nb are 9.34 and 7.83 g/cm^2 respectively[6]. Using an average initial mass of 4.2136g and 3.7612g for the Mo and Nb based alloys respectively, areas of 2.845 and 2.966 cm^2 are obtained. Using the mean initial compositions given in Table I, the composition-time profiles are calculated using Eqns. 3 and 4. These calculated curves are shown in Figs. 1, 2, 3 and 4.

The agreement is considered quite good especially when the degree of experimental scatter and the variability of thermochemical data are considered (see, for example, values published in Hultgren et al.[7]).

The overall prediction of the calculations are also accurate enough for the design of most refining operations. This is a major conclusion of this work.

b) Solution Behavior

In order to more closely examine the small difference between the calculated rates and the experimentally determined rates, the theory will be used to analyze the experimental data to arrive at experimental values of p_A and p_B(or $k_{H,B}$). In the last three columns of Tables II and III, values of α, p_A and p_B are calculated from the initial and final mass, the initial and final composition, and the time for each experiment. For the pure metals, p_A is calculated from the expression

$$p_A = -k_A \frac{dn_A}{dt} \tag{5}$$

and, of course, p_B and α are meaningless. The mean and standard deviation of these values are given in Table IV. These means also have been used as parameters to calculate the curve of "best fit" for the experimental data shown in Figs. 1 through 4 using Eqns. (3) and (4).

For the Nb and Nb-Mo samples, the experimental values are the same as the values obtained from JANAF within the limits of the experimental scatter. This is, in essence, the reason for the previous claim of good agreement. However, assuming that the JANAF value for pure Mo is correct, there is a slight trend towards the experimental value of p_B(or $k_{H,B}$) being low. Hence one might conclude that $k_{H,B} \neq p_B$ for Mo in Nb at 2900K, that $k_{H,B} = 3.4 \times 10^{-5}$ atm, and that the solution exhibits slight negative deviation from ideality. This means in

TABLE IV - Summary of Means and Standard Deviations of P_A, P_B and α Obtained from Experiments

		P_A(atm)	P_B (atm)	α
2900K	Nb	$3.901 \pm 0.521 \times 10^{-6}$		
	Nb-2 w/o Mo	$4.176 \pm 0.748 \times 10^{-6}$	$3.437 \pm 1.009 \times 10^{-5}$	0.131 ± 0.036
	Nb-5 w/o Mo	$3.839 \pm 0.650 \times 10^{-6}$	$3.353 \pm 1.070 \times 10^{-5}$	0.130 ± 0.053
	Nb-Mo (JANAF)	3.890×10^{-6}	4.395×10^{-5}	0.090
3000K	Mo	$8.945 \pm 0.728 \times 10^{-5}$		
	Mo-1 w/o Zr	$9.077 \pm 0.639 \times 10^{-5}$	$2.006 \pm 0.246 \times 10^{-4}$	0.437 ± 0.072
	Mo-5 w/o Zr	$9.385 \pm 0.388 \times 10^{-5}$	$1.903 \pm 0.230 \times 10^{-4}$	0.485 ± 0.042
	Mo-Zr (JANAF)	1.002×10^{-4}	1.556×10^{-4}	0.628

effect that the purification rate of Mo from Nb is slightly slower than if the solution were ideal.

For the Mo and Mo-Zr alloys there is a small but statistically significant difference between the experimentally determined values of p_A and p_B and JANAF. Assuming the solution is dilute enough, deviations from ideality cannot explain the difference for component A. Hence, for p_A one concludes that the value of the vapor pressure of pure Mo is slightly high in JANAF. This may also account for the previous result for Nb-Mo alloys rather than the slight negative deviation from ideal solution behavior postulated. For p_B(or $k_{H,B}$) the experimental value is higher than JANAF. Again assuming that JANAF value for pure Zr is correct, there is a positive deviation from ideality; i.e., $k_{H,B}$ at 3000K for Zr in Mo is 2×10^{-4} atm. This means in effect that the purification rate of Zr from Mo is slightly faster than if the solution were ideal.

There is, however, another interesting possibility for the slightly enhanced rate of purification of Zr from Mo which has previously been described[8]. The presence of O as ZrO_2 in the alloy can have a considerable effect. If ZrO_2 is immiscible in the alloy, the effect is negligible. However, if as little as 10 ppm O present as ZrO_2 is dissolved into the Mo-Zr liquid alloy, interactions of the type originally treated by Paule under this contract, can easily account for enhanced rates of apparent Zr loss of the magnitude observed here. Complications of this sort are better studied using a detailed analysis of vapor species present during evaporation than with the techniques used in this work.

It should be noted that changes in purification rate caused by deviations from ideality are usually only significant in marginal cases where $\alpha \sim 10^{-1}$ or greater. When $\alpha \sim 10^{-3}$ enormous deviations from ideality are required to effect the purification process significantly. In marginal cases, however, extreme care must be taken with regard to details like solution behavior and possible effects of other impurities.

References

1. Paule, R. C., NBSIR 73-402, 33 (1973).
2. Paule, R. C., Boettinger, W. J., Biancaniello, F. S., NBSIR 74-611, 24 (1974).
3. Paule, R. C., Boettinger, W. J., Biancaniello, F. S., NBSIR 76-980, 22 (1976).
4. Darken, L. S., Gurry, R. W., Physical Chemistry of Metals, McGraw-Hill Book Co., New York (1953).
5. JANAF Thermochemical Tables, Dow Chemical Co., Midland, Mich. (1975).
6. Smithells, C. J. ed., Metals Reference Book, fifth edition, Butterworth & Co., London (1976).
7. Hultgren, R., Orr, R. L., Anderson, P. D., Kelley, K. K., Selected Values of Thermodynamic Properties of Metals and Alloys, John Wiley & Sons, New York (1963).
8. Paule, R. C., Boettinger, W. J., Evaporative Purification Processes, "Materials Processing in a Microgravity Environment," Conference Lehigh University, Bethelehem, Pa., Oct. 15-17, 1975, (unpublished).

Appendix

FORM NBS-348
(12-65)

U.S. DEPARTMENT OF COMMERCE
NATIONAL BUREAU OF STANDARDS
WASHINGTON, D.C. 20234

September 8, 1976

REPORT OF ANALYSIS

To: W. Boettinger

Subject: Determination of Molybdenum in Niobium-Molybdenum Alloys.

Method: Atomic Absorption Spectrometry (AAS)

Procedure: Transfer test portion to Teflon beaker. Add 10 ml of water and cover the beaker with Teflon lid. Add 10 ml of HF and then slowly add 5 ml of HNO_3. After sample is dissolved, evaporate solution to approximately 5 ml and transfer to 100-ml plastic volumetric flask. Determine molybdenum by AAS using a nitrous oxide-acetylene flame. To prevent ionization, add 100 µg of K to standard and unknowns. Check the recovery by the standard addition method.

T. C. Rains
T. C. Rains, Chemist

T. J. Brady
T. J. Brady

T. J. Brady for
I. L. Barnes, Chief
Analytical Spectrometry Section
Analytical Chemistry Division

cc: P.D.LaFleur
R.W.Burke

FORM NBS-348
(12-65)

U.S. DEPARTMENT OF COMMERCE
NATIONAL BUREAU OF STANDARDS
WASHINGTON, D.C. 20234

January 3, 1977

REPORT OF ANALYSIS

To: W. Boettinger

Subject: Determination of Zirconium in Molybdenum-Zirconium Alloys

Method: Flame Emission Spectrometry with Repetitive Optical Scanning (FES)

Procedure: Transfer test portion to a Teflon beaker. Add 15 ml of HCl, 5 ml of HNO_3, 2 ml of HF and digest on hot plate until sample is dissolved. Transfer solution to 100 ml plastic volumetric flask and dilute to calibrated volume. Since nitrate interferes in the atomic emission of zirconium, transfer a 10 ml aliquot into a 50 ml beaker and evaporate solution to dryness. Add 5 ml of HCl and repeat the evaporation. Add 5 ml of HCl and warm to dissolve the solids. Transfer the solution to a 10 ml volumetric flask and dilute to calibrated volume with 10 M HCl. Then transfer an aliquot of the sample which contains 20-40 µg Zr/ml to a volumetric flask. Add 1000 µg K/ml and dilute to calibrated volume. Determine the zirconium concentration by FES using a nitrous oxide-acetylene flame. To prevent ionization, add 1000 µg K/ml to standard solutions. Also, add molybdenum to standard solutions to match the matrices. Check the recovery by the standard addition method.

T. C. Rains

T. C. Rains, Chemist

I. L. Barnes

I. L. Barnes, Chief
Analytical Spectrometry Section
Analytical Chemistry Division

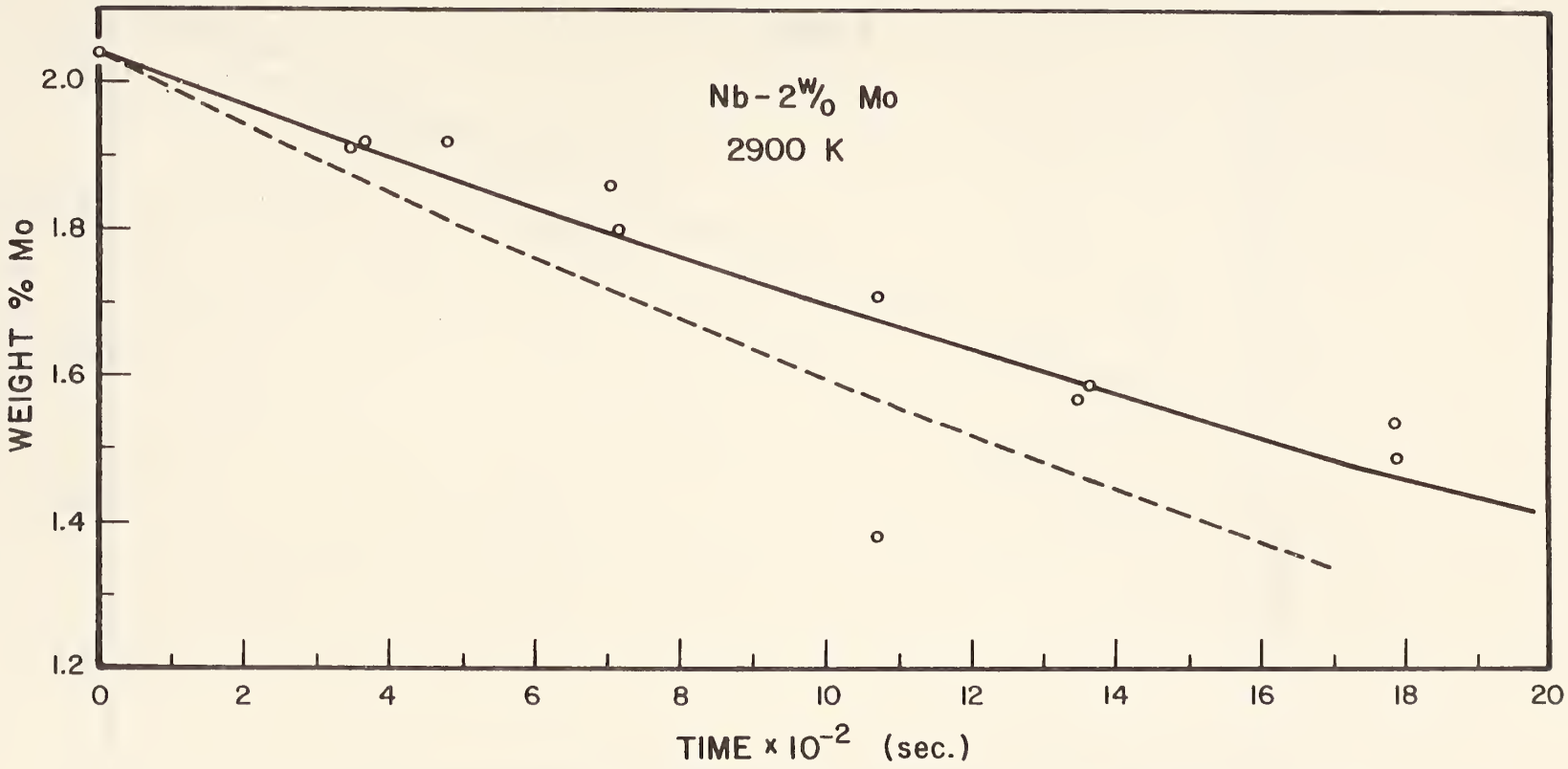

Fig. 1. Plot of composition versus time at temperature for the Nb-2.04 w/o Mo series. The solid line represents the best fit of the data while the dashed line represents the calculated values.

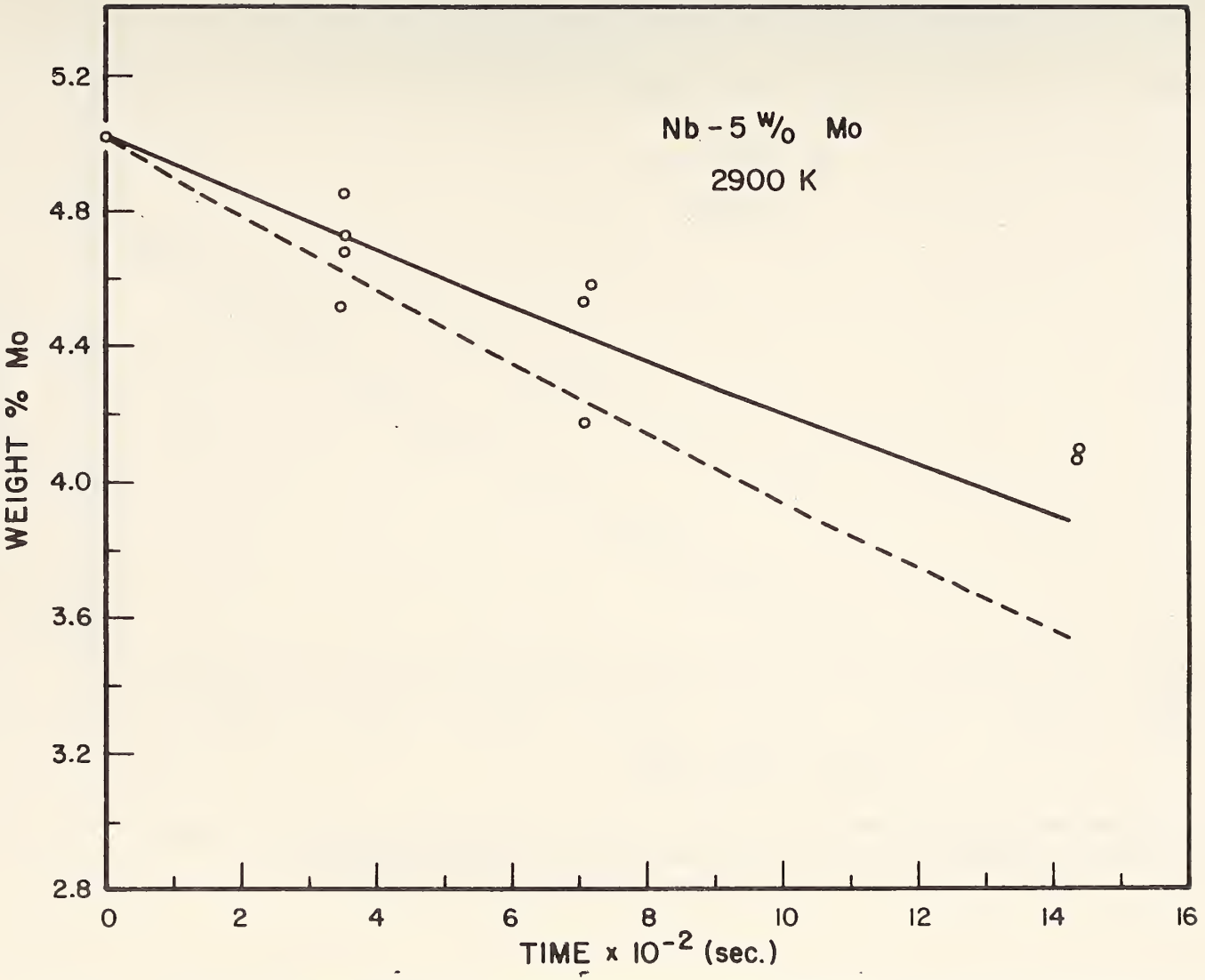

Fig. 2. Plot of composition versus time at temperature for the Nb-5.02 w/o Mo series. The solid line represents the best fit of the data while the dashed line represents the calculated values.

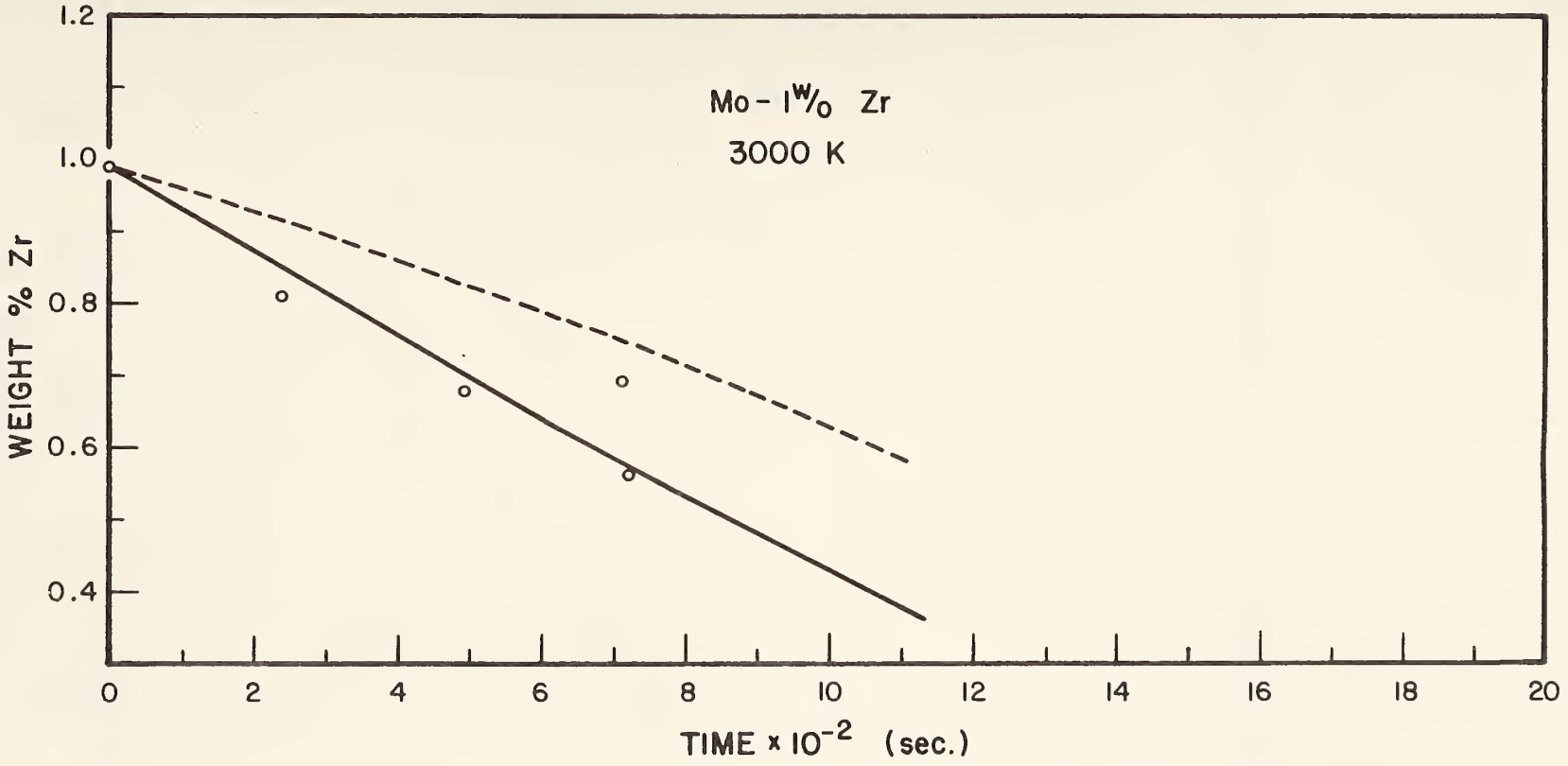

Fig. 3. Plot of composition versus time at temperature for the Mo-0.99 w/o Zr series. The solid line represents the best fit of the data while the dashed line represents the calculated values.

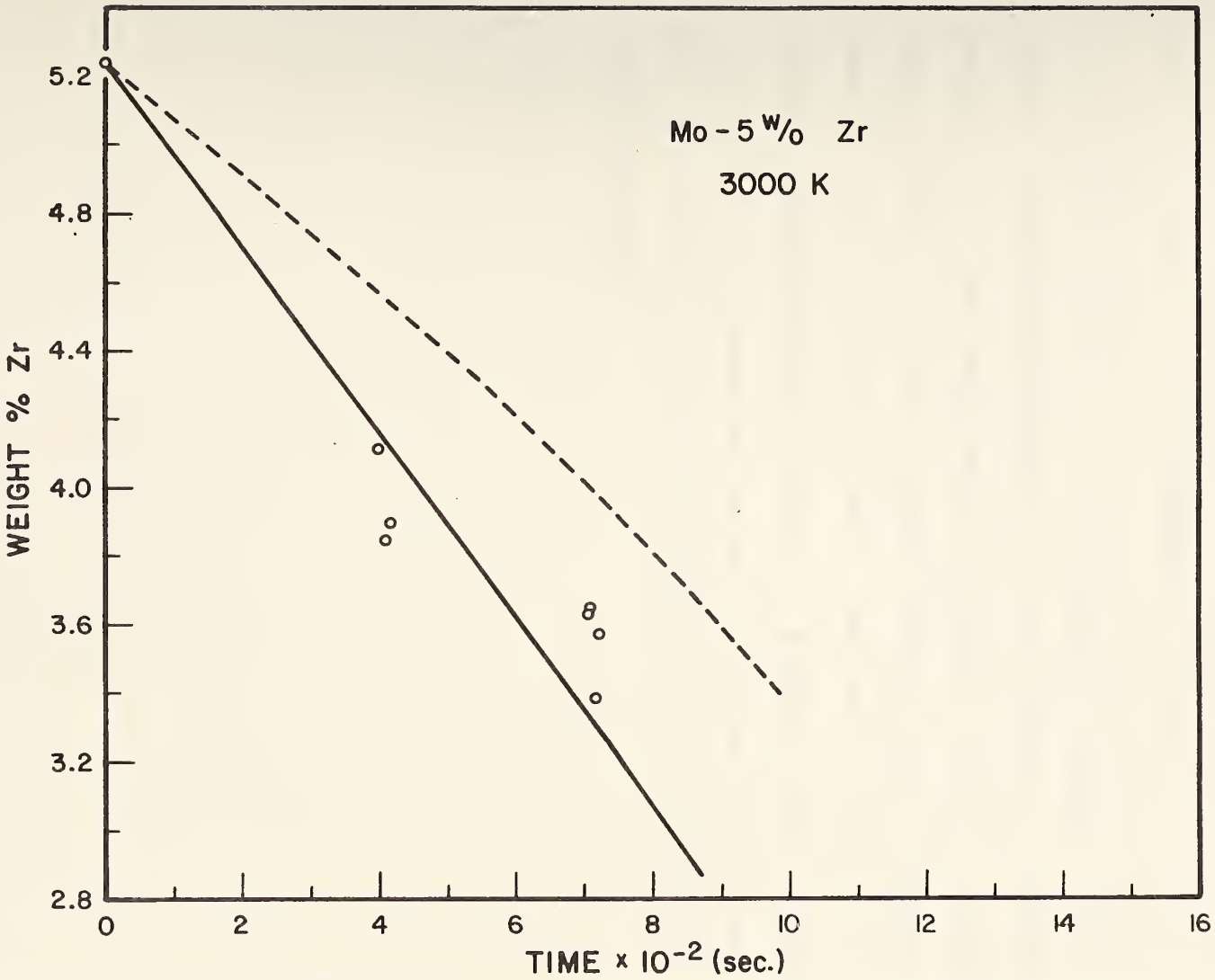

Fig. 4. Plot of composition versus time at temperature for the Mo-5.24 w/o Zr series. The solid line represents the best fit of the data while the dashed line represents the calculated values.

Task 3

VAPOR TRANSPORT SYNTHESIS AND CRYSTAL GROWTH

H. S. Parker

Inorganic Materials Division
Institute for Materials Research

SUMMARY

Attempts to increase the size of mercurous chloride crystals grown by evaporation-condensation in a static system are described. Because of the simple experimental arrangement, the static technique should be useful for growth of small crystals of this and similar materials of suitable vapor pressure. The growth of large (1.5 cm diameter) mercurous chloride crystals by a vapor Bridgman technique is described. Spontaneous nucleation is a problem with both techniques and the use of inert gas to help control the problem should be investigated further.

Introduction

The major objective of this study has been the investigation of advanced techniques for vapor transport crystal growth and definition of the limitations imposed by convective effects in a temperature gradient, for comparison with results of similar experiments in near zero-gravity conditions. The theory and applications of the vapor growth technique have been described by several authors [1,2,3]. Mass transport in the presence of a temperature gradient can be achieved either by the addition of a suitable transporting agent, generally a halide, or by a simple evaporation-condensation mechanism. The presence of the transporting agent necessitates consideration of the reversible reaction occurring at both source and growth end of the transport tube, and separation of these effects from other growth parameters is often difficult. In the case of an evaporation-condensation process, independent control of the total pressure in the system is lost because the vapor pressure of the material is fixed by the operating temperature.

The work described in this report is a continuation of the study of the growth of mercurous chloride by an evaporation-condensation mechanism as described in the previous report [4].

Experimental Procedures

The ampoule loading procedure and growth furnaces have been described previously [4,5]. During this period, both static growth experiments with no relative motion between transport tube and gradient and vapor

Bridgman growth experiments with the tube either lowered or raised through the temperature gradient were performed.

The modified transport tube [4], using an evacuated annular space as thermal insulation at the growth end with a fused silica rod to provide an axial heat flow path [Figure 1], was used for the majority of growth experiments. A few runs were made using growth tubes containing a small reentrant thermocouple well at each end in an attempt to more closely monitor the actual temperature gradient within the tube.

In order to examine the effect of an inert gas on nucleation and growth rate, a series of runs were made with the transport tubes back filled with argon at partial pressures calculated to be 0.1 to 0.5 atmospheres at the average growth temperature. The corresponding mercurous chloride pressure is of the order of 0.9 to 1 atmosphere.

Experimental Results

In view of the success obtained with the modified transport tube described previously [4], attempts were made to increase crystal size in the static system. Runs were made under the same conditions utilized previously, a source temperature of 355°C and a ΔT of 15°C (Δp = 0.15 atm) over the last 6 cm of transport distance. The charged tube was placed in the cold furnace and raised to temperature over a 6 hour period, maintaining the temperature gradient during heating. Inside diameters of the tubes used in the growth region were 8, 10 and 12 mm. Transport times ranged from 16 to 26 hours. In no case was the quality of the resulting boule comparable to that previously

obtained in a 6 mm growth tube. The deposit was coarsely polycrystalline in every case and control of nucleation and interface stability remain obvious problems. Figure 2 shows the development of a polycrystalline deposit during initial stages of a run. In addition to the growing deposit, many smaller crystals can be seen on the tapering walls of the growth tube.

Five growth runs were made using the transport tubes with reentrant thermocouple wells at the source and growth ends of the tube. The source temperature was maintained at 390°C with the growth end 8-10°C cooler ($\Delta p \sim 0.2$ atm). Excessive scatter in transport rates and polycrystalline growth was observed.

Because of the limited success attained in increasing the size of single crystals of mercurous chloride grown in a static system, it was decided to utilize the vapor Bridgman technique. Previous work at NBS [6] was done in a geometry favoring convection, but no attempts were made to determine maximum growth rates or to estimate the magnitude of the convective contribution to transport rates.

Using the vapor Bridgman technique, and the modified transport tube, mercurous chloride crystals larger than 1.5 cm diameter were grown. The crystal shown in Figure 3 was grown at a rate of 0.1 mm per hour, with a furnace temperature of 380°C, corresponding to a mercurous chloride pressure of about 0.9 atmospheres. Results obtained both in a maximum convective configuration (tube raised through gradient) and minimum convective configuration (tube lowered through gradient)

were comparable, using 1 cm I.D. growth tubes and growth rates of 0.1 to 0.15 mm per hour. The maximum rate consistent with reasonable crystal quality for the condition of minimum convection is in the range of 0.15 to 0.2 mm/hr. This rate is not significantly greater than the rates observed in a maximum convection arrangement.

The results of vapor Bridgman growth runs made using argon back-fill pressures in the range of 0.1 to 0.5 atmospheres at growth temperatures of 380° - 385°C (mercurous chloride pressure 0.9 to 1 atmosphere) were inconclusive. Growth rates were varied from 0.1 to 0.3 mm/hr and no effect on nucleation or quality was observed.

Conclusion and Discussion

During the course of this project, the evaporation-condensation crystal growth of mercurous chloride has been investigated using both a static system and a vapor Bridgman technique. Crystals up to 0.6 cm x 1 cm of good quality have been produced by the static technique. Attempts to produce large, bulk single crystals by this technique were unsuccessful, due to spontaneous nucleation. Because of its simple experimental arrangement, the static technique should be useful for growth of this and similar materials of suitable vapor pressure within the size limitations. The vapor Bridgman technique is much more successful for the growth of large single crystals by evaporation-condensation, although growth rates of 0.1 mm/hr or less are necessary for high quality specimens.

In the application of both techniques, spontaneous nucleation on the walls of the growth chamber remains a problem and the investigation of the effect of an inert gas on the growth process should be investigated further.

References

[1] a) H. Schafer, "Chemical Transport Reactions", Academic Press, New York, 1964.

b) H. Schafer in "Preparative Methods in Solid State Chemistry", P. Hagenmuller, Ed., 251-277, Academic Press, New York, 1972.

[2] E. Kaldis, in "Crystal Growth, Theory and Techniques, Volume I", C. H. L. Goodman, Ed., 49-191, Plenum Press, New York, 1974.

[3] M. M. Faktor and I. Garrett, "Growth of Crystals From the Vapor", John Wiley and Sons, New York, 1974.

[4] E. Passaglia and R. L. Parker, "NBS Space Processing Research", NBSIR 76-980, 120-130, February 1976.

[5] E. Passaglia and R. L. Parker, "NBS Space Processing Research", NBSIR 74-611, 69-78, November 1974.

[6] R. A. Forman, W. S. Brower and H. S. Parker, "Mercurous Chloride Polarizer Material", AFML-TR-74-56, April 1974.

Figure 1. Modified growth tube. Annular space between growth tube and outer tube evacuated for thermal insulation. Heat flow path is 3 mm fused silica rod connecting tubes at left end.

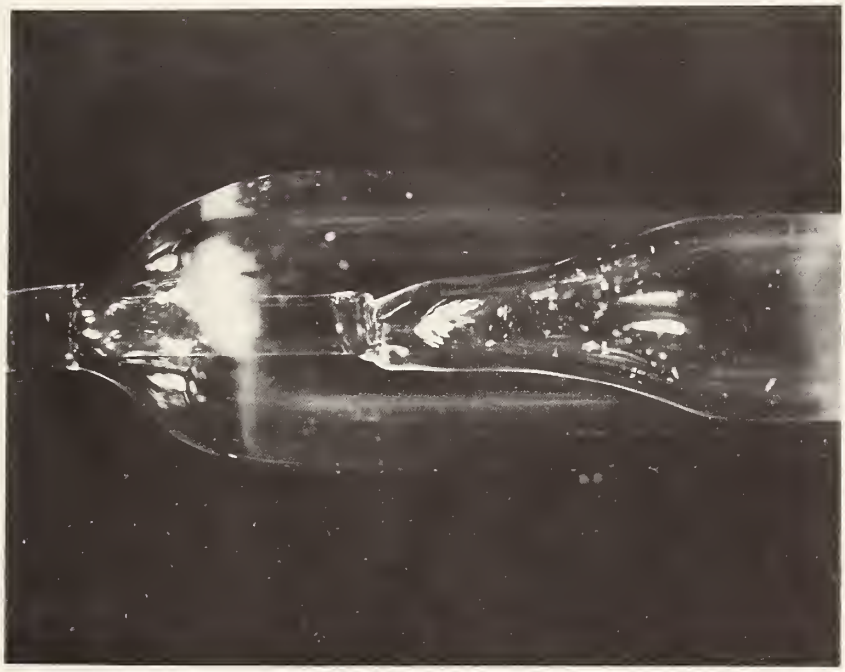

Figure 2. Polycrystalline deposit of mercurous chloride during initial stages of growth run.

Figure 3. Single crystal of mercurous chloride grown by vapor Bridgman technique.

Task 4

Melt Shape in Weightless Crystal Growth

S. R. Coriell, S. C. Hardy

Metallurgy Division
Institute for Materials Research

and

M. R. Cordes

Applied Mathematics Division
Institute for Basic Standards

Summary

We have made measurements of the motions of air bubbles in a viscous silicone oil as determined by buoyancy and thermocapillary forces. The oil is contained in a small cell across which a linear temperature gradient is established. This temperature gradient causes the surface tension to vary over the air-oil interface of a small bubble at the center of the cell. As a consequence, Marangoni convection develops in the oil and the bubble experiences a thermocapillary force. We have measured the gradient required to generate a thermocapillary force which just balances the buoyancy force and thus stabilizes the bubble. A plot of this gradient as a function of bubble diameter is in excellent agreement with the theoretical behavior predicted by solving the Navier-Stokes equations in the creeping flow approximation. Measurements of bubble velocity away from equilibrium are also in agreement with theory.

The shape of axisymmetric liquid zones and their stability with respect to axisymmetric perturbations has been investigated numerically. For growth of constant diameter crystals by the floating zone process, the necessary boundary conditions are prescribed freezing radius R_f,

melting radius R_m and meniscus angle ϕ_f at the freezing interface. For these boundary conditions with $R_f=R_m$ and fixed length L to radius ratio, the maximum value of the gravitational field for which such a liquid zone exists is calculated. Under certain conditions, it is found that there exist two different zone shapes which satisfy the boundary conditions.

The processing of materials in space will involve free liquid surfaces. These free surfaces may be intentional as in processes analogous to floating zone or Czochralski or may develop unexpectedly as bubbles form or the liquid separates from the container wall. If surface tension gradients are established on these free surfaces, Marangoni convection may develop and spread throughout the volume. Recent calculations[1] have indicated that such convection can be quite vigorous even for small gradients in some situations. Thus an understanding of surface tension driven fluid flow is important to the proper design and interpretation of space experiments and processes. We have started experimental studies of Marangoni convection in the past year and will report some measurements in part A of this report. An understanding of the shape and stability of liquid zones is also essential to the development of a microgravity materials processing technology. We have continued our work in this area and part B of this report will discuss some new results.

A. Marangoni Convection Studies

Introduction

We have initiated studies of Marangoni convection this past year with measurements of the motion of air bubbles in a viscous silicone

oil in response to buoyancy and thermocapillary forces. This problem was selected because its theoretical analysis is relatively simple compared to other geometries and had already been developed.[2] The analysis considers a fluid sphere of radius R and density ρ' immersed in a second fluid of density ρ. A temperature gradient G in the bulk liquid results in a variation of tension over the interface. This surface tension gradient produces a tangential sheer stress at the interface which sets the fluid into motion both inside and outside the bubble as illustrated in figure 1. Usually the variation of surface tension with temperature, $\gamma' = d\gamma/dT$, is negative and the fluid flows from hot to cold at the interface. As a result the bubble experiences a thermocapillary force opposite to the fluid flow, i.e. from cold to hot.

In the approximation of creeping flow the linearized Navier-Stokes equations describe the fluid flow and the temperature fields reduce to solutions of Laplace's equation. The appropriate boundary conditions on the stress, temperature, and heat flux result in an expression for the velocity of the bubble.

For air in silicone oil, $\rho' << \rho$, $\mu' << \mu$ and $k' << k$ where μ and k are the viscosity and thermal conductivities respectively and the prime denotes the bubble fluid. In this case the expression for the bubble velocity becomes

$$v = \frac{1}{3\mu}\left[\rho g R^2 - \frac{3}{2}\gamma' R G\right] \quad (1)$$

where the first and second terms in the bracket give the effects of the volume buoyancy and surface tension forces respectively. The coordinate

system is chosen so that the positive direction is upward. Since $\gamma' < 0$, there is a $G_o < 0$ at which the thermocapillary force and the buoyancy force are in balance so that the bubble is motionless. In this case, we have

$$G_o = \frac{\rho g D}{3\gamma'} \qquad (2)$$

where D=2R. Thus a plot of G_o as a function of D is linear, passes through the origin and has slope $\frac{dG_o}{dD} = \frac{\rho g}{3\gamma'}$, assuming ρ and γ' are constant. For values of $G < G_o$, the bubble will move downward; for $G > G_o$, the bubble will move upward.

Experimental Apparatus and Procedures

The earlier paper (2) in which the above theory was developed also presented the results of some measurements of G_o as a function of bubble diameter for silicone oils. The experimental results are so scattered, however, that only general agreement with theory is indicated. These experiments used uncontained oil zones held between the end pieces of a micrometer by capillarity. The temperatures of the end pieces were controlled with small heaters wound about copper blocks in contact with the micrometer shafts; the temperatures were measured with thermometers thrust into these blocks. The temperature measurement and control were, consequently, not precise and the optical observations were affected by the curved surface of the zone. In addition, the large uncontained air-oil interface of the zone probably gave rise to a general Marangoni convection which may have affected the motion of bubbles even near the axis where observations were made.

To avoid these obvious experimental problems, we constructed the simple device shown in Figure 2. The oil is contained in the small rectangular cell (A) which has flat double glass windows in front and back and insulated sides. The top (B) and bottom (C) surfaces of the cell are brass plates which are soldered to tubes wound with small nichrome heaters (D, E,). The top plate rests on narrow spacing strips of plastic which give the cell a depth of about 0.3 cm. At this depth, the fluid viscosities and negative gradients employed in these experiments give calculated Raleigh numbers far below the value required for convection due to density variations; no convection could be detected from observations of small particles in the absence of a bubble. Miniature thermocouples (F, G) pass through the plates and are cemented to the top and bottom surfaces near their centers. The heaters are controlled by variable transformers connected to a constant voltage source. The thermocouples are read with a millivoltmeter whose output drives a strip chart recorder. In operation, the cell temperatures after adjustment of the heaters were constant to about 1°C for several hours. The top heater was usually not used. Instead, the top temperature was held nearly constant by blowing compressed air over the uninsulated brass tube.

The linearity of the temperature gradient in the cell was checked by inserting a microthermocouple (.003" wire) through a small side tube (H) thus permitting temperature measurements at three points. The results are shown in figure 3 where the temperature differences given by the three thermocouples are plotted as a function of their positions for various gradients. These data show that the temperature distribution

in the cell was linear at gradients higher than any used in bubble motion measurements.

To avoid complications arising from possible interactions and perturbations of the flow fields, measurements were made with only one bubble in the cell. Single bubbles were inserted in the middle of the cell through the side tube (H) using a microliter syringe. Figure 4 shows a bubble shortly after ejection from the syringe as it drifts upward. The bubbles are observed and photographed through a microscope equipped with a micrometer eyepiece.

Experimental Results

In the introduction the motion of air bubbles in a viscous fluid was treated as the result of buoyancy and thermocapillary forces. In our experiments the behavior is more complicated than this model suggests because the bubble radius is generally changing due to the temperature dependent solubility of air in silicone oil. Since the temperature varies with position in the cell, the solubility also varies. Although the oil is initially undersaturated with air, when the temperature gradient is established, the oil is supersaturated near the bottom where it is hot while remaining undersaturated at the top. Thus an air bubble at the top of the cell will shrink and at the bottom of the cell it will grow. For a given gradient and air concentration there is only one temperature i.e. one location in the cell at which a bubble can be at equilibrium with the silicone oil.

The changes in bubble radius caused by the position dependent solubility give rise to complicated bubble motions. For most experiments

the temperature gradient in the cell is fixed and the bubble when inserted is usually sufficiently large for the buoyancy force to exceed the thermocapillary force. Consequently the bubble will move upward and come to rest against the top plate. It is now in the coolest area of the cell and the oil is undersaturated with air; the bubble will be shrinking. Eventually the radius will become sufficiently small for the thermocapillary force to exceed the buoyancy force and the bubble will detach from the top plate and move downward. It will continue to shrink as it decends until it passes the solubility equilibrium point and moves into the region of supersaturated oil where it will begin to grow. Usually the radius will become large enough to make the buoyancy force dominant before the bottom plate is reached and the bubble will reverse its motion and ascend to the top of the cell. For the same air concentration and a different gradient, the bubble may completely dissolve before passing the position of solubility equilibrium on its first descent. Alternatively, for a certain range of gradients, the bubble motion and diameter will fluctuate with almost sinusoidal regularity. This oscillatory mode is shown in figure 5 where bubble position Z and diameter D are plotted as a function of time over one cycle.

One of the major goals of these experiments was to measure the gradients required to make bubbles motionless. The size fluctuations discussed above, although seeming to complicate the experiments, make available a simple technique for these stabilizing gradient measurements with the important feature that the cell gradient can remain constant during the measurement. All that is necessary is to record the bubble diameter when the motion reverses, either in rising or descending. At

the direction reversal the velocity is zero and the buoyancy and thermocapillary forces are equal. The reversal point is easily determined using the micrometer eyepiece and the bubble is photographed to measure the diameter. Figure 6 shows the bubble diameter at reversal as a function of temperature gradient. A line through the points passes through the origin and has a slope which give $\gamma' = .055 \frac{mJ}{m^2 K}$. If a γ' is calculated for each point using eq. 2, we find $\gamma'_{Avg} = .053 \frac{mJ}{m^2 K}$ with a standard deviation of $\pm .002 \frac{mJ}{m^2 K}$. This γ' is about 10% lower than the $.061 \frac{mJ}{m^2 K}$ value (probable error of 10%) found by direct measurement [2]. Thus the observations of bubble diameter as a function of stabilizing gradient are in agreement with theoretical predictions; the scattered results of the earlier work were the result of the non ideal experimental conditions.

We have also made some measurements of bubble velocities in order to compare with the theoretical predictions expressed in Equation (1). This was undertaken because the viscosity dependence of the bubble velocity drops out at $v=0$ thus reducing the problem to a special case. The agreement between calculated and measured velocities was not good. However, this is to be expected because the calculation of V requires the subtraction of two terms which are nearly the same. A better way to compare measurement and theory is to use the measured velocity along with the gradient and bubble radius in equation 1 to calculate a valve of γ'. The calculation requires a determination of the temperature of the bubble so that the proper value of the viscosity may be used. This is easily determined from the known gradient and the position at which the velocity is measured. The velocity is measured by determining

Z as a function of time and finding the slope at the desired point to get $v=\frac{dZ}{dt}$. Table 1 shows the results of such measurements with some isothermal bubble velocity data. The average calculated value of γ' is about .052 $\frac{mJ}{m^2K}$, in good agreement with the results of the zero velocity measurements.

Discussion

These observations of air bubble motion in response to buoyancy and thermocapillary forces seem to be in excellent quantitative agreement with the predictions of theory for the fluid flow velocities used. Several incidental observations, however, are worth noting. It was evident from early measurements not shown here that the behavior of bubbles at and near the top and bottom plates was somewhat different from the behavior in the center of the cell. The difference was evidenced in slightly higher values of γ' than those reported here. Some deviation from center cell behavior was anticipated because of the obvious disturbance to the fluid and temperature fields by the rigid surfaces. In addition, some observations were made of bubble interactions. These were appreciable in the case of two bubbles of greatly different size. It appeared that the convection field of the larger bubble could influence the motion of the smaller bubble at large distances i.e. several large bubble diameters. This indicated that the flow velocities were significant at some distance from the interface generating the convection. Observations of the motion of small particles contained in the silicone oil support this conclusion.

Part B - Shape and Stability of Liquid Zones

In connection with modelling the floating zone process we have continued our studies [3] of the shape and stability of liquid zones. In addition, in collaboration with Dr. T. Surek of Mobil-Tyco Solar Energy Corporation, we have developed a theory which predicts the time evolution and stability of the dimensions of the solidifying crystal during the floating zone process.

The shape and stability of liquid zones has been discussed extensively in previous annual reports. In this report we will emphasize new developments and results. We consider a liquid zone of length L between two solids which are circular cylinders (plates) and are coaxial. The radii of the upper and lower plates are R_u and R, respectively. Defining the usual cylindrical coordinate system $(\bar{r}, \theta, z)$ with origin midway between the two solids and coaxial with them, we study the effects of a constant gravitational acceleration g along the negative z-axis and of rotation with constant angular velocity Ω about the z-axis. We assume that the liquid-vapor interface is axisymmetric and denote the shape by the function $\bar{r} = r(z)$. This assumption is consistent with the direction of the gravitational field and the axis of rotation. We assume that the wetting behavior of the liquid is such that $r(-L/2)=R$ and $r(L/2)=R_u$ are appropriate boundary conditions. For a static (or uniformly rotating) liquid, the liquid-vapor interface shape is given by the Laplace capillary equation, viz.,

$$\gamma\{r^{-1}(1+r_z^2)^{-1/2} - r_{zz}(1+r_z^2)^{-3/2}\} = -\rho gz+(\rho\Omega^2 r^2/2)+p. \quad (3)$$

where γ is the liquid-vapor surface tension, ρ is the density difference between liquid and vapor, p is a constant (Lagrange multiplier), and

the subscript z indicates differentiation with respect to z i.e., $r_z \equiv dr/dz$.

In our previous annual report [3], results for the shape and stability of liquid zones were presented based on numerical solutions of the Laplace capillary equation and the associated Jacobi differential equation. The numerical method failed whenever $|r_z|$ became too large. To avoid this difficulty, we have rewritten the equations in terms of arc length t. Defining

$$r' = \sin \phi \qquad (4)$$

$$z' = \cos \phi \qquad (5)$$

where the prime indicates differentiation with respect to t, i.e., $z' = dz/dt$. The Laplace capillary equation is then

$$\phi' = [\cos(\phi)/r] + (\rho g z/\gamma) - (\rho \Omega^2 r^2/2\gamma) - (p/\gamma). \qquad (6)$$

The Jacobi equation is obtained from the Laplace capillary equation by letting $z \to z + \delta z$, $r \to r + \delta r$, $p \to p - (\mu/2)$. and $\phi \to \phi + \delta\phi$. Retaining only linear terms in the variational quantitities δr, δz and $\delta\phi$, we find

$$W'' + (\sin\phi/r)\, W' + W \{\phi'^2 + \cos^2\phi/r^2 + (\rho g/\gamma)\sin\phi + (\rho\Omega^2 r/\gamma)\cos\phi\} = \mu/2\gamma, \qquad (7)$$

where $W \equiv \cos\phi\, \delta r - \sin\phi\, \delta z$; this is the Jacobi equation. The stability criterion is [4]

$$t^* > t_m \qquad (8)$$

where the conjugate point t* is the first positive root of the equation

$$u(t^*) \int_o^{t^*} v\, r\, d\, t - v(t^*) \int_o^{t^*} u\, r\, d\, t = 0 \qquad (9)$$

The origin of arc length has been chosen such that $r(0)=R$, $z(0)=-L/2$ and $r(t_m)=R_u$, $z(t_m)=L/2$. The functions u(t) and v(t) are non-trivial solutions of the homogeneous ($\mu=0$) and inhomogeneous ($\mu \neq 0$) Jacobi equation which vanish at t=0. The arc length formulation allows us to treat zones which are not representable by a single valued function r (z), i.e., we can now consider zone shapes such that there are two or more values of r for a given value of z.

The Laplace capillary equation is solved as an initial value problem. At present the computer program can consider two types of boundary conditions. For fixed L, ρ, γ, g and Ω, type I finds a solution for specified values of R, R_u and volume V, while type II obtains a solution for specified values of R, R_u and $\phi_i \equiv \phi(0) = \arctan [r_z\ (z=-L/2)]$. The program has been written so that it will be relatively easy to incorporate other types of boundary conditions; only type I was available in the previous computer program. For type I boundary conditions, the solution is obtained by guessing values of ϕ_i, p, and t_m and iterating to obtain values of ϕ_i, p and t_m which give the desired values $r\ (t_m)=R_u$, $z(t_m)=L/2$, and volume V. The iteration on t_m is not strictly necessary but was introduced for programming convenience. For type II boundary conditions, ϕ_i is specified so that the iteration is only on p and t_m. The iteration method is similar to that previously used. In testing for stability of the solution only axisymmetric perturbations which conserve the zone volume are considered. For zone shapes representable as r(z), it has been shown [5] that one need only consider axisymmetric perturbations to determine stability. It is also known [6] that under some circumstances axisymmetric menisci become unstable with respect to asymmetric perturbations. Thus, for zone shapes not representable by a single valued function r(z), it will be necessary to consider stability with respect to asymmetric perturbations. At present we have not attempted this.

Before discussing the numerical results, we will briefly describe a theory of shape stability of the dimensions of the solidifying crystal in the float zone process. For greater detail the reader is referred to

reference 7. We consider the following floating zone system; a solid cylinder S_f of radius R_f is grown by melting a solid cylinder S_m of radius R_m. The liquid zone of volume V is between the solids S_f and S_m, which are being moved at velocities v_f^* and v_m^*, respectively. At the S_f - liquid interface solid is freezing at a rate v_f, while at the S_m - liquid interface solid is melting at a rate v_m. The basic equations for the time evolution of the system are

$$\dot{L}=(v_m - v_m^*) - (v_f - v_f^*), \qquad (10)$$

$$\dot{V}=\pi(\rho_s/\rho_L)\ (R_m^2 v_m - R_f^2 v_f), \qquad (11)$$

$$\dot{R}_f=v_f \tan\ (\phi_f - \phi_o), \qquad (12)$$

$$\phi_f=f\ (V, L, R_f, R_m). \qquad (13)$$

The first equation expresses the change in zone length L as a function of the pulling velocities v_m^* and v_f^* and the freezing and melting velocities. The dot indicates differentiation with respect to time τ. The second equation represents the change in zone volume due to the freezing and melting process; ρ_s and ρ_L are solid and liquid densities, respectively. The third equation describes the dependence of the change in freezing radius on the meniscus angle ϕ_f at the freezing interface. For the floating zone geometry previously described with the lower interface as the freezing interface, ϕ_f is identical to ϕ_i, viz, $\phi_f=\phi(0)=$ arctan $[r_z(z=-L/2)]$. Results for the upper interface freezing can be obtained by changing the sign of the gravitational acceleration. The angle ϕ_o is a property of the material and is the meniscus angle necessary for constant radius growth, i.e., $\phi_o=\phi_f$ for $\dot{R}_f=0$. For silicon, recent measurements [8] indicate that $\phi_o=11°$. The final equation expresses $\phi_f=\phi_i$ as a function of the zone variables V, L, R_f and R_m; the dependence on

ρ, γ, g and Ω is not explicitly indicated. The functional relationship is found by solving the Laplace capillary equation as previously described. It should be pointed out that the Laplace capillary equation assumes a static liquid (a uniformly rotating liquid can be taken into account). In the actual floating zone process there is certainly Marangoni convection due to temperature gradients (and on earth gravity driven convection). The effects of such convection on zone shape remains to be investigated.

We [7] have carried out a perturbation treatment to test the stability of the steady state solution of the above equations. At steady state $\dot{L} = 0$, $\dot{V} = 0$, $\dot{R}_f = 0$ and $\phi_f = \phi_o$. We denote small deviations from steady state by the symbol Δ; e.g., $\phi=\phi_o+\Delta\phi$, $R_f=R_{fo}+\Delta R_f$, etc., where a subscript $_o$ denotes the steady state value. Upon writing the above equations in terms of the perturbed quantities and neglecting any non-linear terms, we obtain a set of three linear inhomogeneous equations for the quantities ΔV, ΔR_f and $\Delta\phi_f$. An important assumption in this procedure is that the freezing and melting velocities are functions only of time and are not functions of the variables R_f, R_m, L, V and ϕ_f. Thus we are neglecting thermal effects which would cause v_f and v_m to depend on these variables; future work will consider the thermal fields.

The stability of the dimensions of the crystal is determined by the solution of the homogeneous equations for ΔV, ΔR_f and $\Delta\phi_f$; these solutions are of the form $\exp(\lambda\tau)$. If the real part of λ is negative, the exponential decays with time and the steady state is stable. For the real part of λ positive, ΔV, ΔR_f and $\Delta\phi_f$ increase exponentially with time and the steady state is unstable. It can be shown that the

necessary and sufficient conditions for stability of the dimensions of the freezing crystal are

$$(\partial \phi_o / \partial R_f) < 0 \text{ and } (\partial \phi_o / \partial V) > 0. \qquad (14)$$

For a stable system, it is convenient to write $\lambda = -\alpha \pm i\beta$ where α and β are frequencies of decay and oscillation, respectively. Explicit formulas for α and β are

$$\alpha = -(v_{fo}/2)\ (\partial \phi_o / \partial R_f) \qquad (15)$$

$$\beta = v_{fo}\{2\pi R_{fo}(\rho_s/\rho_L)\ (\partial \phi_o/\partial V) - (\partial \phi_o/\partial R_f)^2/4\}^{1/2} \qquad (16)$$

The derivatives $(\partial \phi_o/\partial R_f)$ and $(\partial \phi_o/\partial V)$, which determine the time evolution and stability of the dimensions of the resolidifying crystal can be determined using the computer program previously described.

The liquid zone shape depends on five dimensionless parameters R_u/R, $V/\pi R^2 L$, L/R, $\varepsilon_R \equiv \rho \Omega^2 R^3/\gamma$ and $\varepsilon \equiv \rho g R^2/[\gamma(1+\varepsilon_R)]$. In the calculations to be discussed we have taken $\Omega = 0$ so that $\varepsilon_R = 0$ and $\varepsilon = \rho g R^2/\gamma$. In our previous annual report we considered in detail the case $R_u/R = 1$ and $V/\pi R^2 L = 1$. Experimental results for water zones in air were presented. Additional experiments on water zones in dibutyl phthalate, which is only slightly soluble in water and is of slightly higher density, using both solid end plates and open tubes, have further confirmed the theory. The comparison of theoretical and experimental results is indicated in Fig. 7. The surface tension of water-dibutyl phthalate was measured by the pendant drop technique and the value of 22.8 m J/m^2 was used in the comparison of theory and experiment.

We have also carried out experiments to determine the maximum stable length as a function of ε for horizontal liquid zones. For this case, there are no exact theoretical results, however, for small ε, one can

obtain an approximate analytic result by expanding the appropriate Euler and Jacobi equations in powers of ε and retaining terms of order ε^2. The basic result [3] for small ε is that the zone is stable when

$$L/R < 2\pi \{1 - (\pi\varepsilon/2)^2 + \ldots.\} . \qquad (17)$$

In Figure 8 we show the experimentally measured L/R values as a function of the Bond number for horizontal zones. The solid line in the figure is the theoretical prediction just stated; the dashed curve is the result for vertical zones shown in Figure 7. The horizontal zones are more stable than the vertical zones for ε less than approximately 0.5.

The present numerical calculations have chiefly been concerned with the liquid zone shapes which permit constant diameter crystal growth, i.e., the angle ϕ_i is in the vicinity of zero. An approximate calculation of zone stability for $\phi_i=0$ has been made by Heywang.[9] We will briefly outline this calculation. We take $\Omega=0$ (no rotation) and consider the case $R=R_u$. For large R (or large Bond number ε), we neglect the term containing r^{-1} on the left hand side of eq (3). The Laplace capillary equation can then be integrated and we obtain

$$r_\eta = h(\eta)/[1-h^2(\eta)], \qquad (18)$$

where $h(\eta)=(\rho g/2\gamma)\eta^2-(\rho/\gamma)\eta$ and $\eta=z+(L/2)$. Note that $r_\eta=0$ and hence $\phi_i=0$ at the freezing interface $\eta=0$ as desired. Further integration yields

$$r(\eta)-R= \int_o^\eta \{h(\bar{\eta})/[1-h^2(\bar{\eta})]\}d\bar{\eta} . \qquad (19)$$

This satisfies the boundary condition r(0)=R; the boundary condition r(L)=R requires that

$$\int_o^L \{h(\eta)/[1-h^2(\eta)]\}d\eta=0, \qquad (20)$$

i.e. p is chosen such that the above equation holds. However if L is sufficiently large that $h^2(L)=1$, the denominator $1-h^2$ of the above expressions vanish; note that this corresponds to an infinite value of r_η, i.e., $\phi=\pm 90°$. Heywang assumes that this corresponds to the largest possible zone length, which we denote by L*. In order to find L* we define $\lambda=(\rho g/\gamma)^{1/2}L^*$ and $x=\eta/L^*$; eq (20) with $p=(\rho g/2)L^* - \gamma/L^*$ becomes

$$\int_0^1 \{g(x)/[1-g^2(x)]\}dx=0, \qquad (21)$$

where $g(x)=(\lambda^2/2)(x)(x-1) + x$. Heywang found that $\lambda=2.84$ satisfied the above equation; Green [10] found $\lambda=2.62$ and our own numerical evaluation yields $\lambda=2.67$. Thus the Heywang approximate calculation yields $L^*=2.67\ (\lambda/\rho g)^{1/2}$ for the largest possible zone length.

In table 2 for $\phi_i=0$ at the lower interface, which is freezing, we give results for maximum zone length based on numerical calculations using the computer program previously described. These zones contain liquid volumes $V < \pi R^2 L$. The zone radius is R at $z=-(L/2)$; the radius decreases to a minimum and then increases reaching R at $z=(L/2)$. For a planar solid-liquid melting interface perpendicular to the zone (z) axis it is impossible for the angle ϕ to be greater than 90° since the liquid-vapor interface would intersect the solid-liquid interface prior to reaching the triple junction of liquid, vapor and solid at $r\ (z=L/2)=R$. Such behavior is illustrated in fig. 9. Thus for $(L^*/R)=1.0$, 0.5 and 0.25, we have used as the criterion for maximum zone length, the value of ε at which $\phi = 90°$ at $z = L/2$. For non-planar solid-liquid interfaces the $\phi = 90°$ criterion is not appropriate; depending on the shape of the solid-liquid interface ϕ could be greater or less than 90°. Our

calculations indicate that zone shapes with $\phi > 90°$ can be stable with respect to axisymmetric perturbations (stability with respect to asymmetric perturbations remains to be investigated). Note that the Heywang approximation, which may be written $(L^*/R)\varepsilon^{\frac{1}{2}} = 2.67$ is excellent for large Bond numbers ε.

For $L^*/R = 6.0$, 4.0 and 2.0 in Table 2, the maximum zone length is determined by a different mechanism, which will now be described. In figure 10 we plot ϕ_i as a function of zone volume for all other variables fixed for two different Bond numbers, $\varepsilon = 1.38$ and 1.50. The interesting and somewhat surprising feature of the $V(\phi_i)$ curve is that a given value of ϕ_i can be obtained for two different volumes. For $\varepsilon = 1.38$ and $-0.1° \leq \phi_i \leq 5.9°$, there are two volumes which give the same ϕ_i. For $\phi_i \geq 5.9°$, there is a unique volume, and a $\phi_i \leq -0.1°$ is not possible for $\varepsilon = 1.38$. For volumes less than those indicated in the figure the liquid zone is unstable with respect to axisymmetric perturbations. As ε increases the $V(\phi_i)$ curve moves to the right as illustrated by the ε=1.5 curve in fig. 10. For ε>1.384 a value of ϕ_i=0 is no longer possible. Thus, as given in Table 2, for ε>1.384 a liquid zone with L/R=2.0 and ϕ_i=0 does not exist. Recalling that one of the criteria for the stability of steady state growth during the floating zone process was $(\partial\phi_o/\partial V)>0$, it is clear that in those cases for which two different volumes give the same ϕ_o one volume corresponds to $(\partial\phi_o/\partial V)$ positive and the other volume to $(\partial\phi_o/\partial V)$ negative. Obviously for constant diameter crystal growth it is highly desirable to use the volume corresponding to $(\partial\phi_o/\partial V)$ positive. For ε=1.25, figures 11 and 12 illustrate two liquid zones with different volumes but both having ϕ_i=0.

Table 3 gives results for maximum zone length for $\phi_i=0$ at the upper interface which is freezing. The calculations are actually carried out by taking $\phi_i=0$ at $z=(-L/2)$ and g negative. These zones contain liquid volumes $V>\pi R^2 L$; a zone shape is illustrated in figure 13. Note that for this particular liquid zone, the magnitude of ϕ at the melting interface exceeds 90°. This zone is not representable as a single valued function r(z). For specified L/R, Table 3 gives the ε value at which the zones become unstable with respect to axisymmetric perturbations. Since it is possible that zones not representable as r(z) first become unstable with respect to asymmetric perturbations, we also give in Table 4, the value of ε, denoted by ε_{90}, at which $|\phi|=90°$ at the melting interface, i.e., for $\varepsilon>\varepsilon_{90}$, the liquid zone is not representable as r(z). As can be seen from Table 3, ε is about 6% greater than ε_{90}. The Heywang approximation $(L^*/R)\varepsilon^{1/2}=2.67$ is very good at large Bond numbers.

In comparing Tables 2 and 3, it is clear that for large ε, the values of ε for a given maximum zone length differ only slightly; the maximum zone length depends only weakly on whether the lower or upper interface is freezing. However, for small ε(L^*/R=4.0 and 6.0) there are order of magnitude differences between the ε values for freezing at the lower and upper interfaces. However, the zone volumes are very different; for $(L^*/R)=6.0$ with the lower interface freezing (Table 2) $V/\pi R^2 L \cong 0.97$ while for the upper interface freezing (Table 3) $V/\pi R^2 L \cong 5.5$. The larger volume greatly increases the stability of the zone. Recall that for $\varepsilon=0$ and $L/R=2\pi$, zones with $V<\pi R^2 L$ are unstable.

TABLE 2

Maximum zone length L* as a function of Bond number $\varepsilon=\rho g R^2/\gamma$; $R_u=R$, $\Omega=0$, and $\phi_f=0$. Lower interface is freezing.

L*/R	ε	$(L^*/R)\varepsilon^{1/2}$
6.0	$4.6(10^{-5})$	0.041
4.0	$5.24(10^{-2})$	0.915
2.0	1.384	2.35
1.0	7.223+	2.69
0.5	28.98+	2.69
0.25	115.3+	2.68

+ Valued of (L*/R) based on $\phi \geq 90°$ at melting interface.

TABLE 3

Maximum Zone Length L* as a function of Bond number $\varepsilon=\rho g R^2/\gamma$; $R_u=R$, $\Omega=0$ and $\phi_f=0$. Upper interface is freezing. ε_{90} corresponds to the Bond number at which the meniscus is horizontal at the melting interface.

L*/R	ε	ε_{90}	$(L^*/R)\varepsilon^{1/2}$
6.0	.1121	.1046	2.01
4.0	.325	.307	2.28
2.0	1.631	1.543	2.55
1.0	7.135	6.728	2.67
0.5	29.555	27.838	2.72
0.25	119.90	112.88	2.74

There are a number of areas for further investigation. The stability of axisymmetric zones with respect to asymmetric perturbations. (e.g., perturbations which correspond to a translation of the zone) is unkown when the zone shape cannot be described by a single-valued function r(z). The maximum zone length when the meniscus angle ϕ_f at the freezing interface is not zero has not yet been systematically studied. The value $\phi_f=11°$ is appropriate for Si crystal growth[8]. A more fundamental and difficult problem is the evaluation of the effect of fluid flow and electromagnetic fields on zone shape and stability. The present calculations assume a static liquid. In actual floating zone systems there will be Marangoni convection due to surface tension gradients and convection due to gravitational forces. In the special case of a uniformly rotating fluid, it is clear that zone shape and stability can be completely modified. However, for the fluid flow present in the floating zone process, the magnitude of the fluid flow effect on zone shape and stability is not known.

We are indebted to H. W. McLaughlin, R. F. Sekerka and T. Surek for helpful comments and discussion.

References

1. Chang, C. E., and Wilcox, W. R., Proceedings of the "International Colloquiem on Drops and Bubbles," 1974, pg. 194.

2. Young, N. O., Goldstein, J. S., and Black, M. J., J. Fluid Mech. 6, 350(1959).

3. Coriell, S. R., Hardy, S. C., and Cordes, M. R., NBS Space Processing Research (NBSIR 76-980) February 1976, p. 99

4. Bolza, O., Lectures on the Calculus of Variations, Dover, New York, 1961.

5. Gillette, R. D. and Dyson, D. C., Chem. Eng. J. 3, 196(1972).

6. Michael, D. H. and Williams, P. G., Proc. R. Soc. London A 351, 117(1976).

7. Surek, T. and Coriell, S. R., J. Crystal Growth, to be published.

8. Surek, T. and Chalmers, B., J. Crystal Growth, 29, 1(1975).

9. Heywang, W., Z. Naturforschg. 11a, 238(1956).

10. Green, R. E., Jr., J. Appl. Phys. 35, 1297(1964).

Table I

G (°C/cm)	T (°C)	R ($cm \times 10^3$)	$v_{obs.}$ ($cm/sec. \times 10^3$)	$v_{calc.}$ ($cm./sec. \times 10^3$)	γ' mJ/m^2k
0	22	8.18	2.05	2.01	
0	23	9.47	2.79	2.86	
0	55	8.24	3.38	3.54	
93.3	37	4.48	5.59	6.54	.051
101.1	34	5.00	5.60	7.15	.050
101.9	37	5.97	5.95	7.00	.052
129.3	45	10.39	3.93	4.62	.054

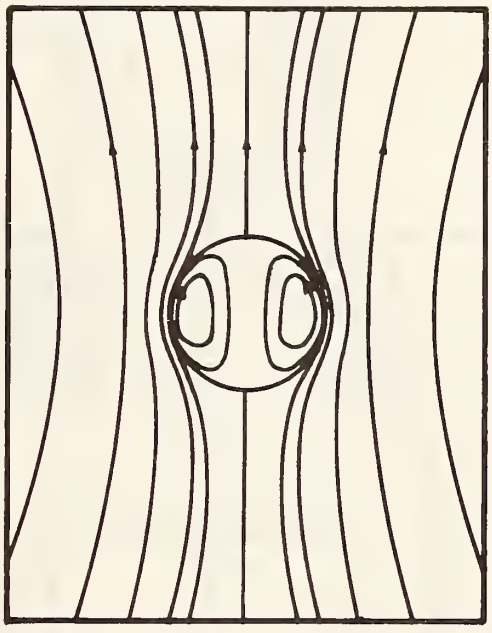

Fig. 1 Fluid flow generated by thermocapillary forces about a sperical interface.

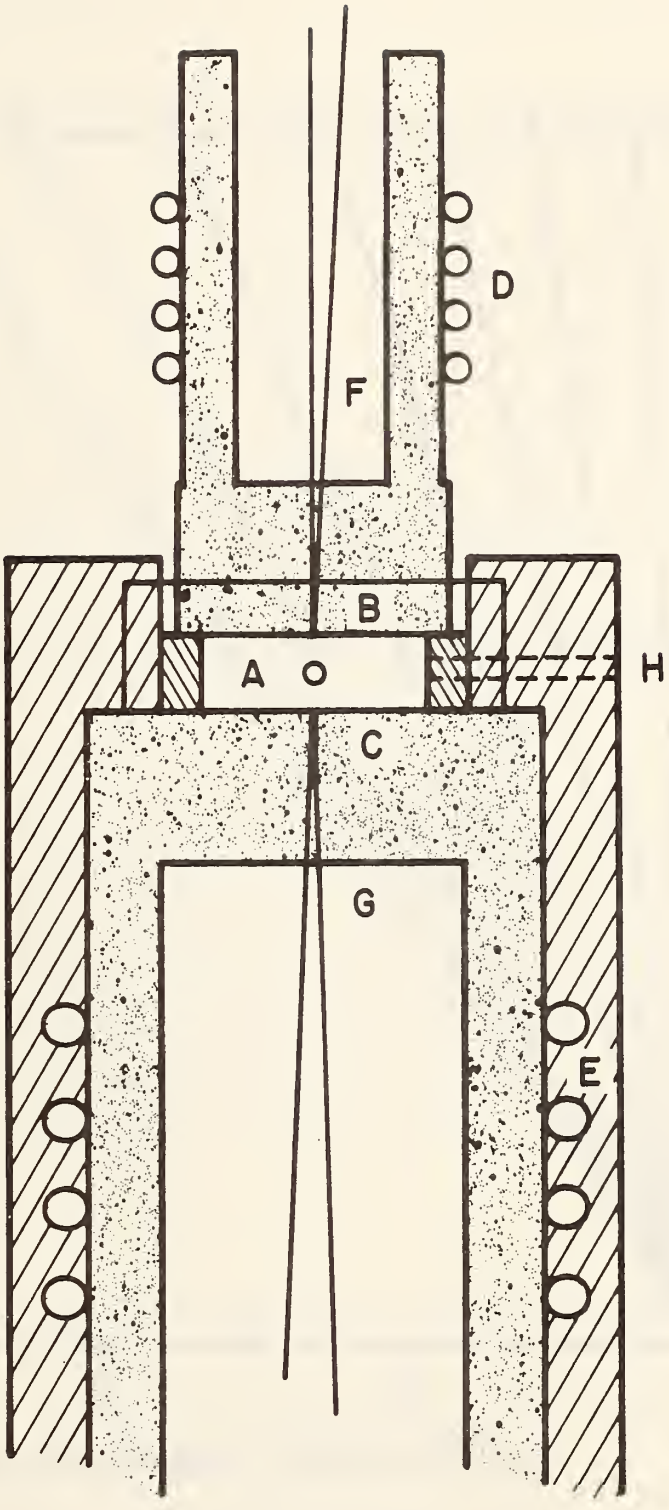

Fig. 2 Temperature gradient cell for studies of bubble motion.

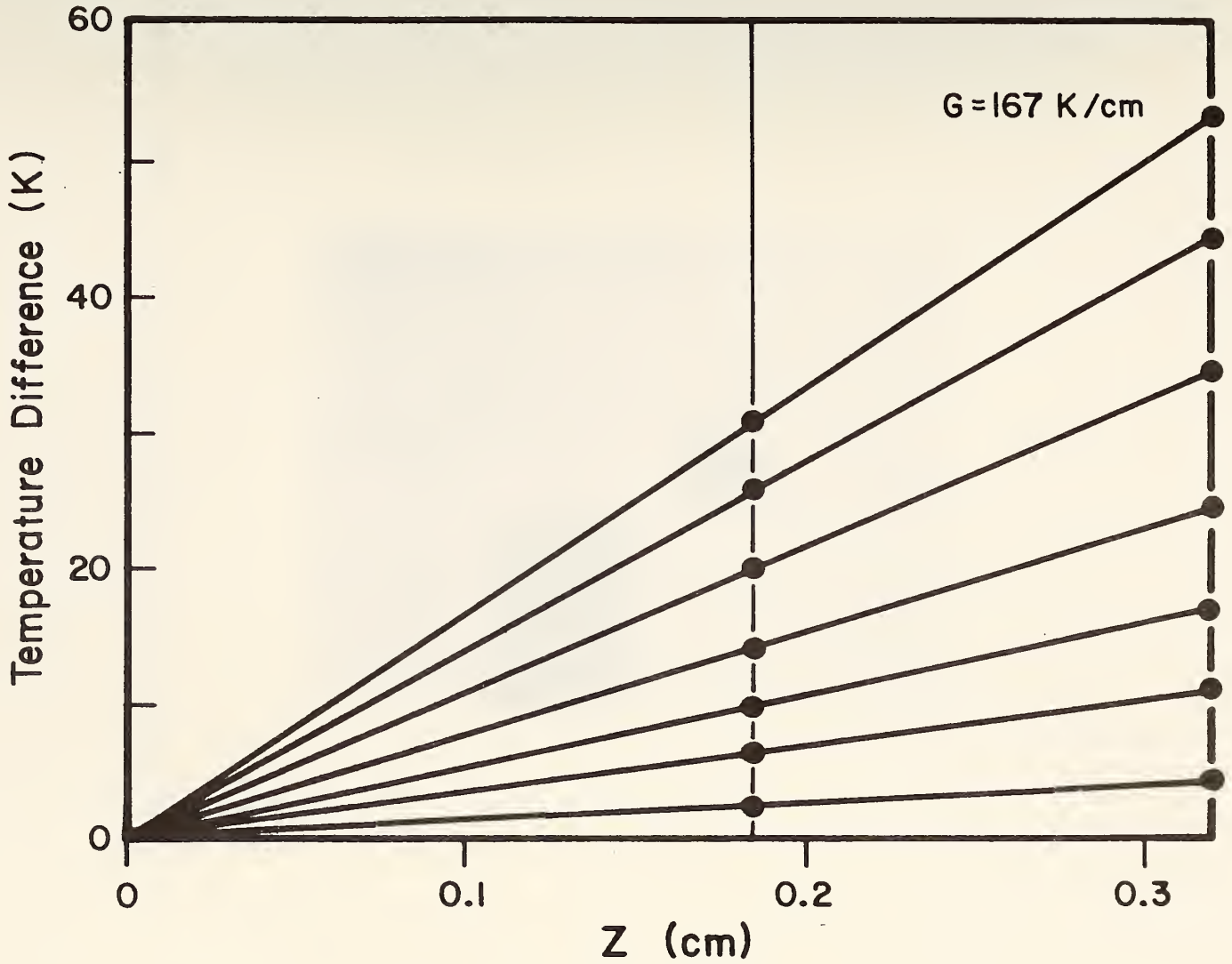

Fig. 3 Temperature distribution in the cell.

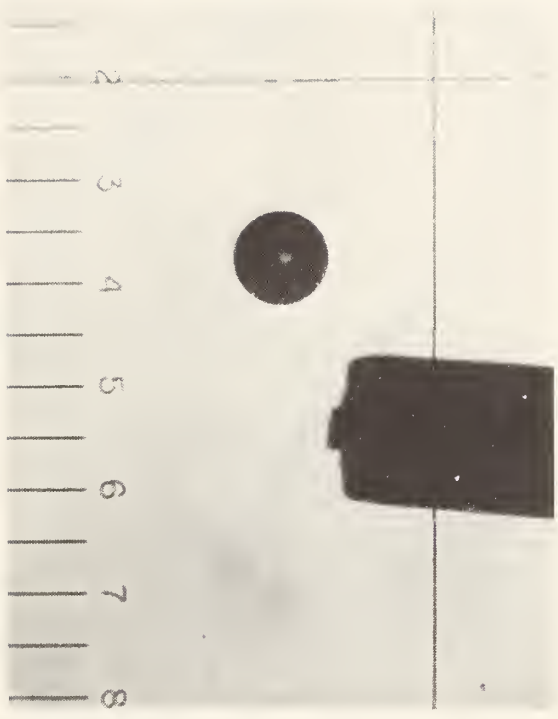

Fig. 4 Bubble shortly after injection into the silicone oil.

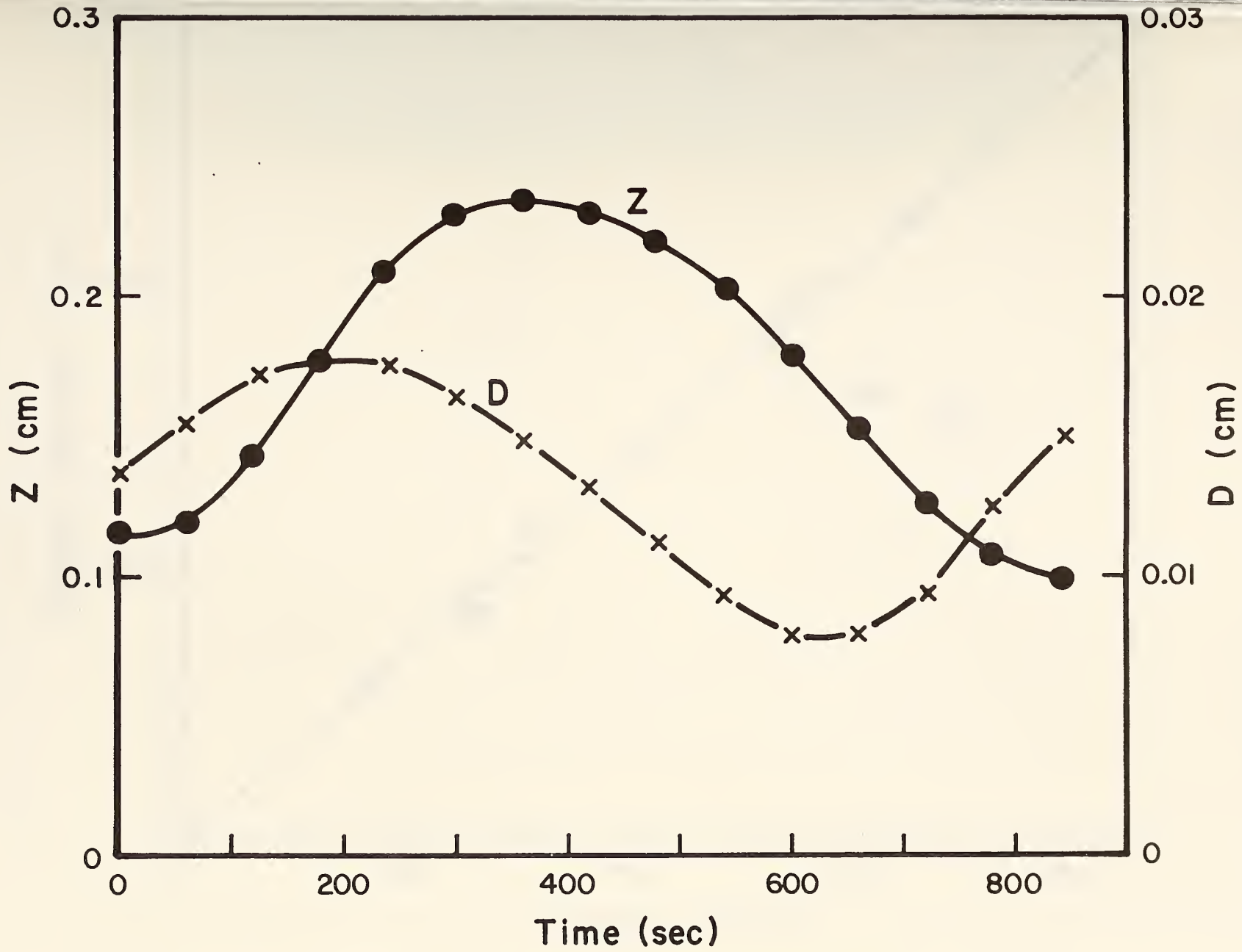

Fig. 5 Oscillations of bubble diameter and position.

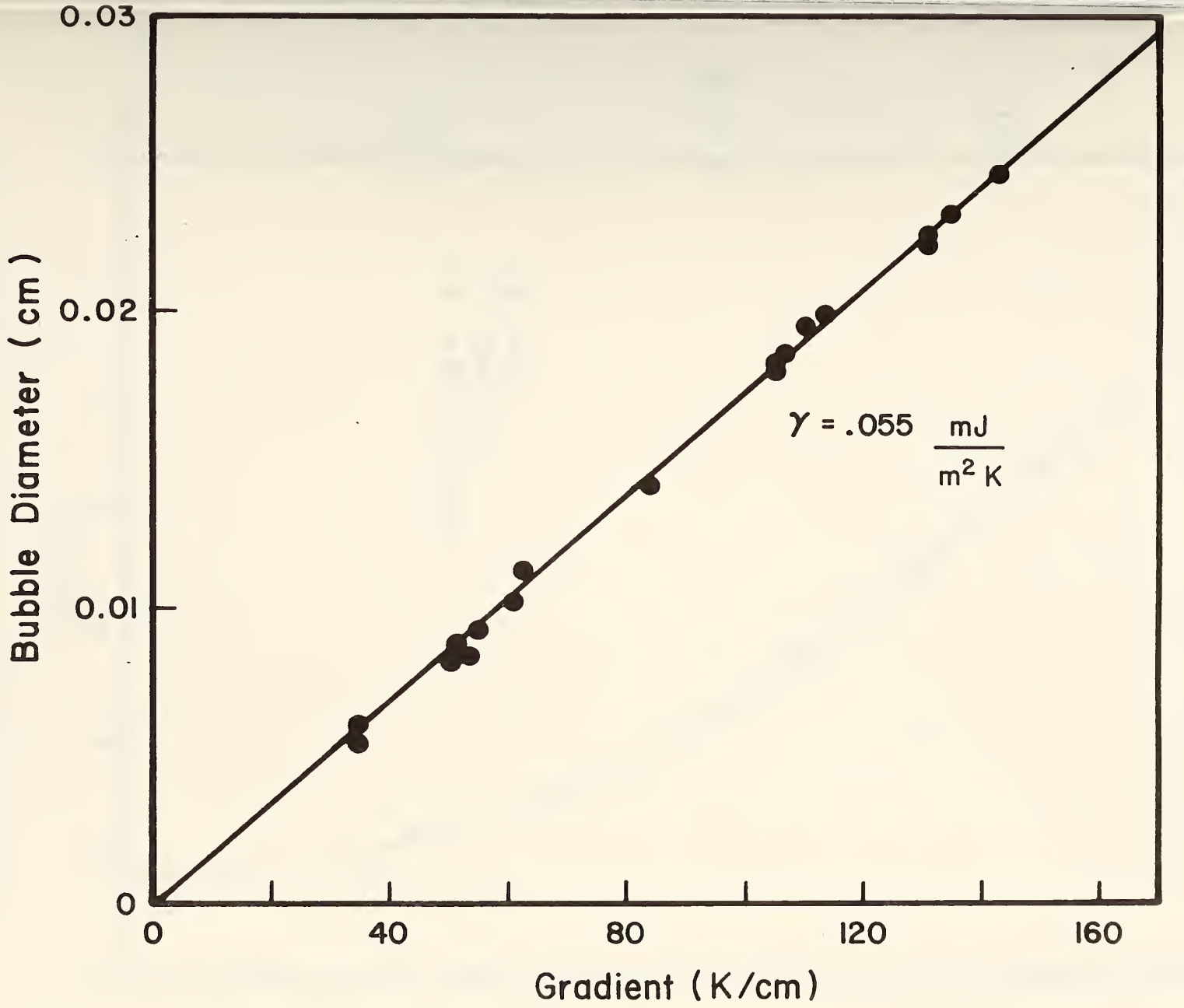

Fig. 6 Bubble diameter at which the velocity vanishes as a function of temperature gradient.

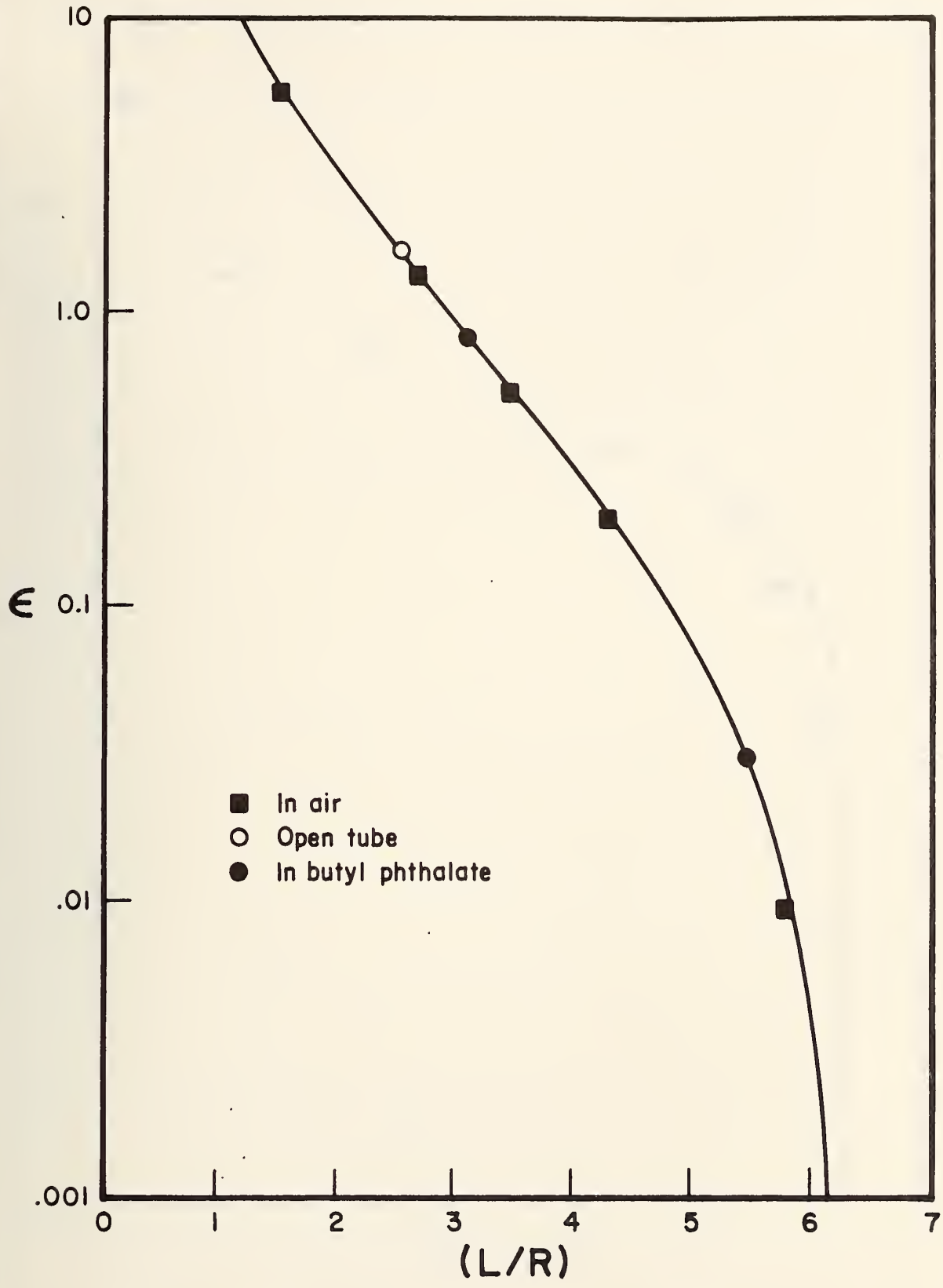

Fig. 7 A comparison of numerical (solid line) and experimental (points) results for the maximum stable zone length (vertical zones) as a function of the Bond number $\epsilon=\rho g R^2/\gamma$.

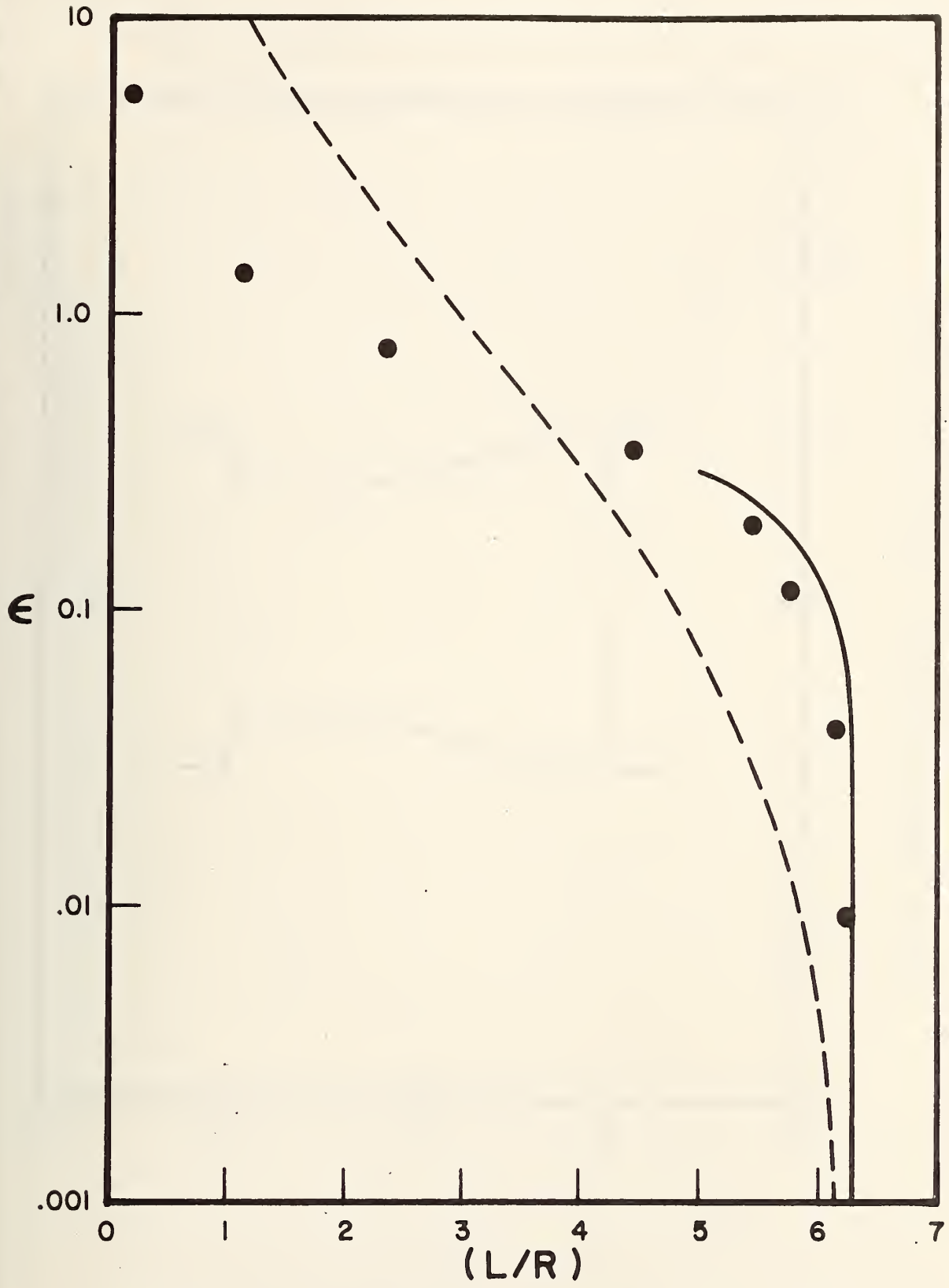

Fig. 8 The circles represent experimental results for the maximum stable zone length (horizontal zones) as a function of ε. The solid line is an approximate analytic result for small ε for horizontal zones. The dashed line represents vertical zones.

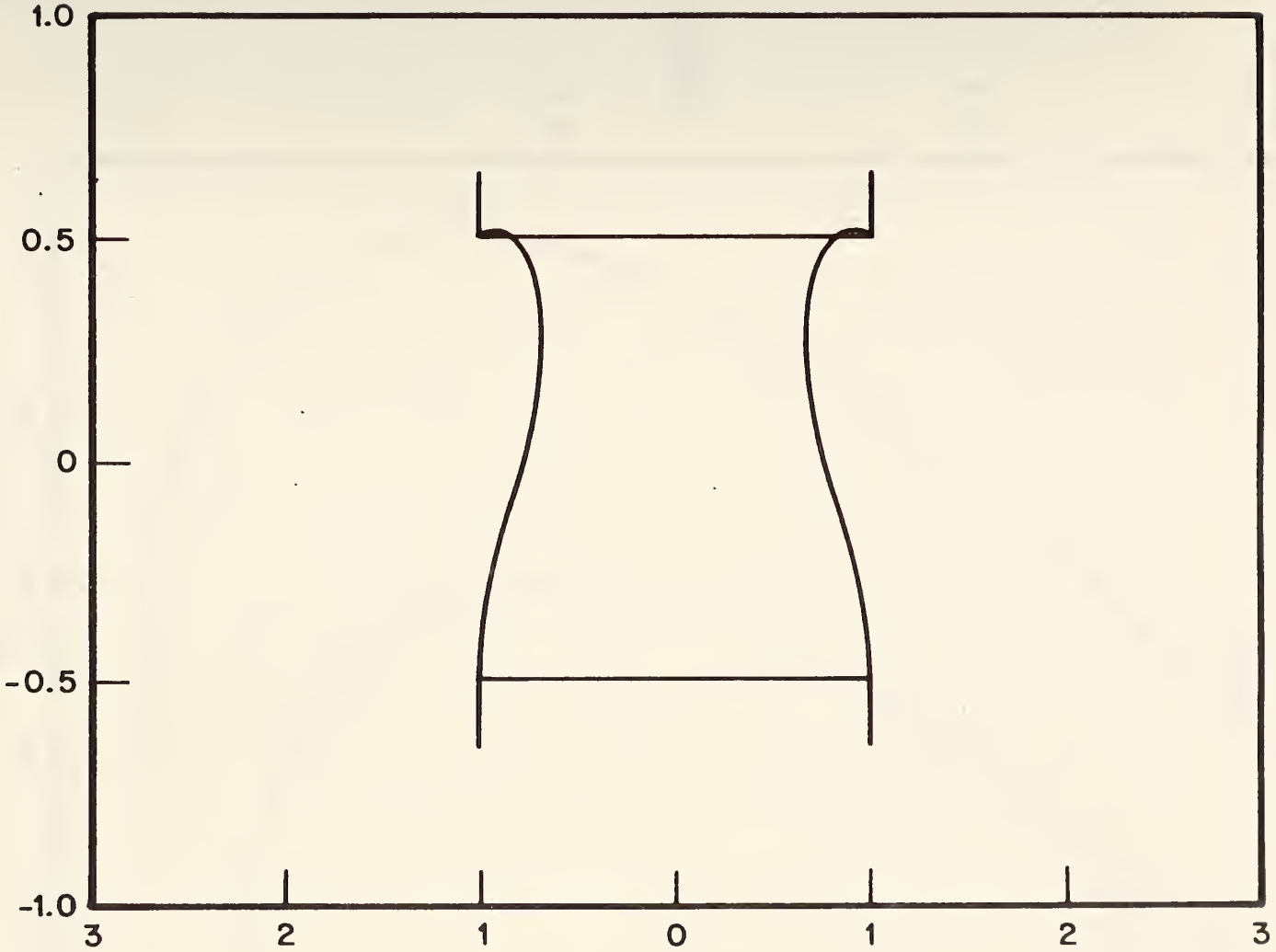

Fig. 9 Liquid zone for $R_u/R = 1.0$, $L/R = 1.0$, $\varepsilon_R = 0$, $\varepsilon = 7.51$, and $\phi_f \equiv 0$. Note that such a zone is impossible if the upper solid-liquid interface is planar.

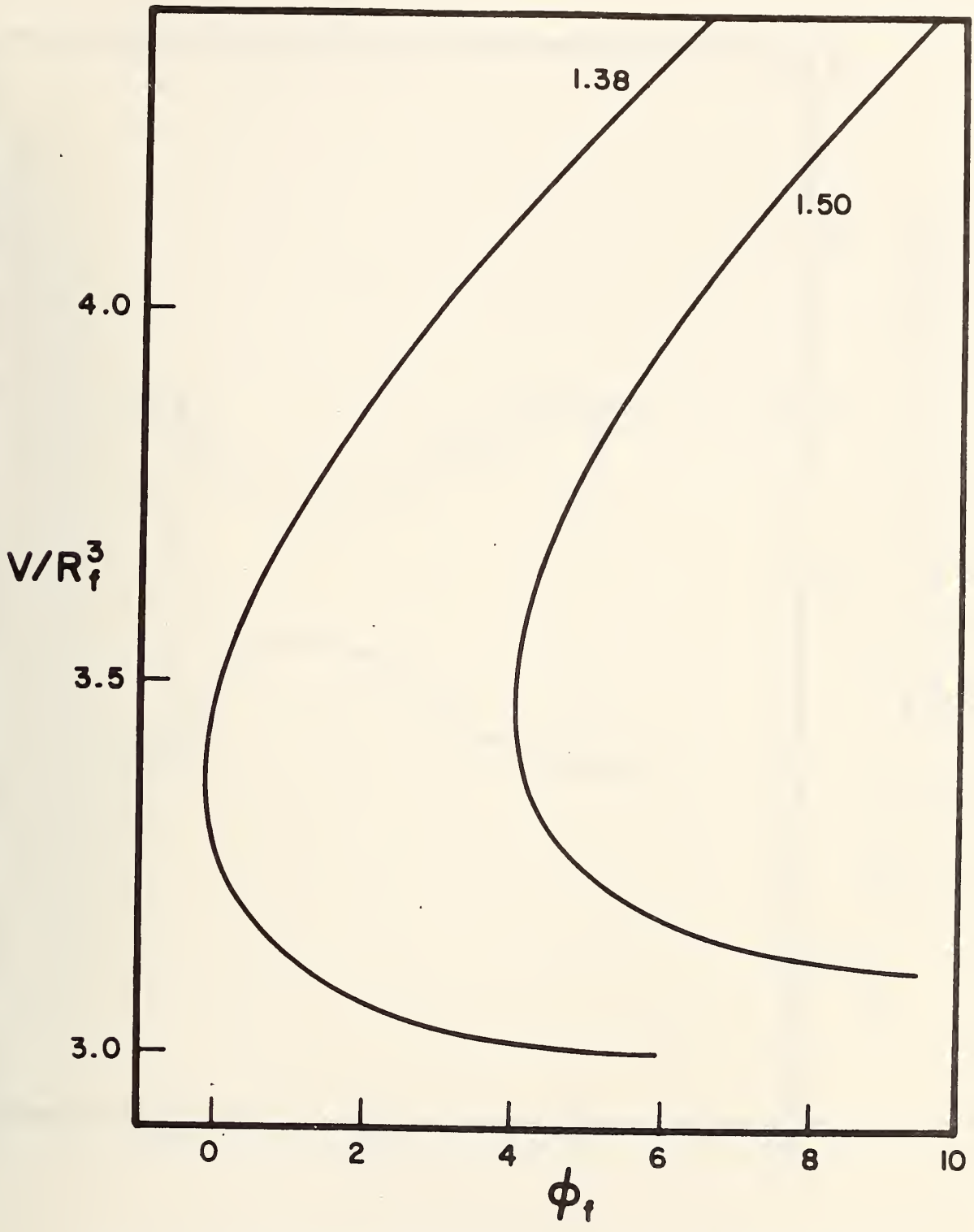

Fig. 10 Liquid zone volume V (in units of R_f^3) a function of ϕ_f (in degrees) for ϵ = 1.38 and 1.50 with R_u/R_f = 1.0, L/R_f = 2.0 and ϵ_R = 0. There may be zero or one or two volumes which give a specified ϕ_f.

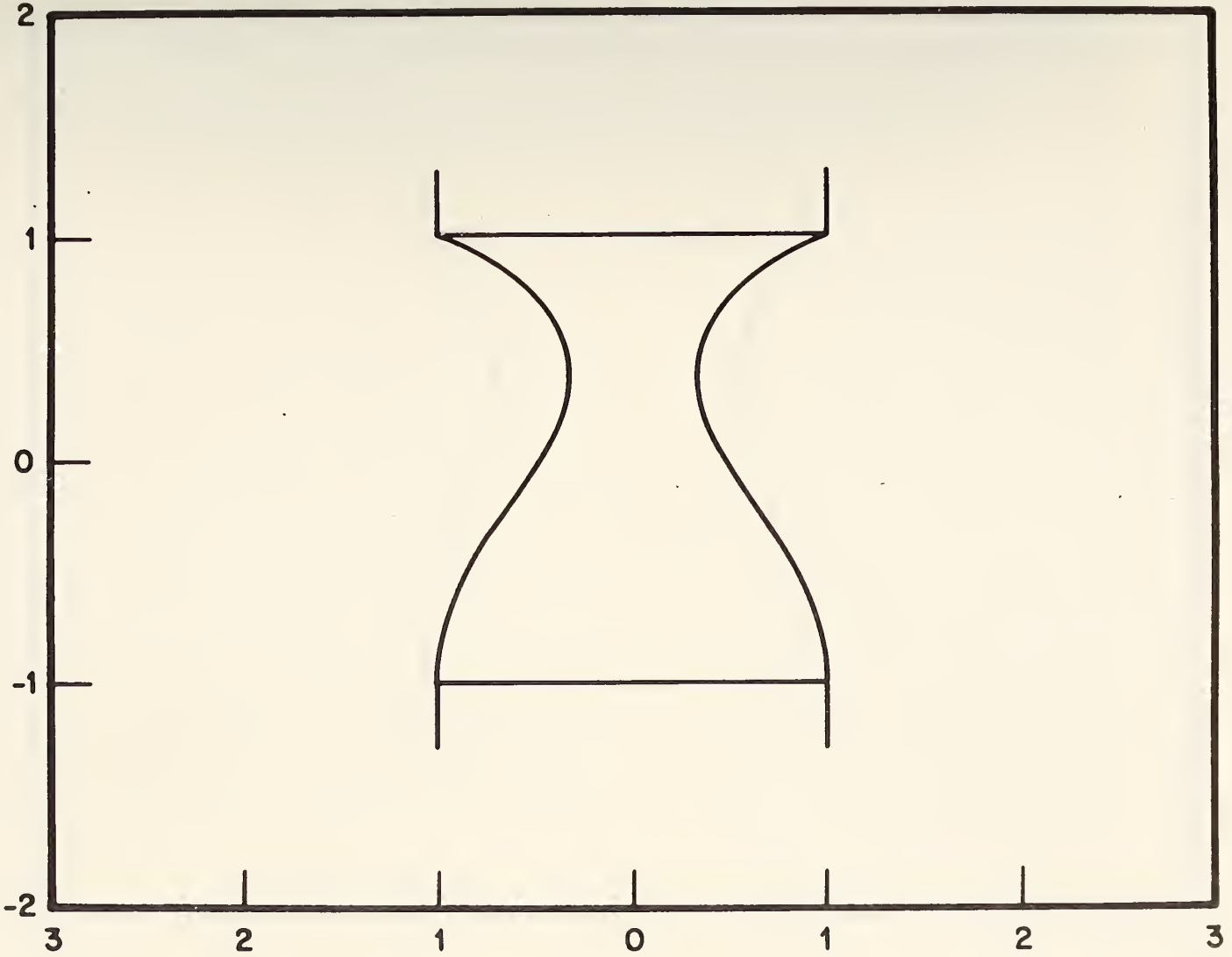

Fig. 11 Liquid zone for $R_u/R = 1.0$, $L/R = 2.0$, $\varepsilon_R = 0$, $\varepsilon = 1.25$ and $\phi_f = 0$. Compare this zone with Fig. 12 which also has these values; for this zone $V/R^3 = 2.9$ while the zone in Fig. 12 has $V/R^3 = 4.0$.

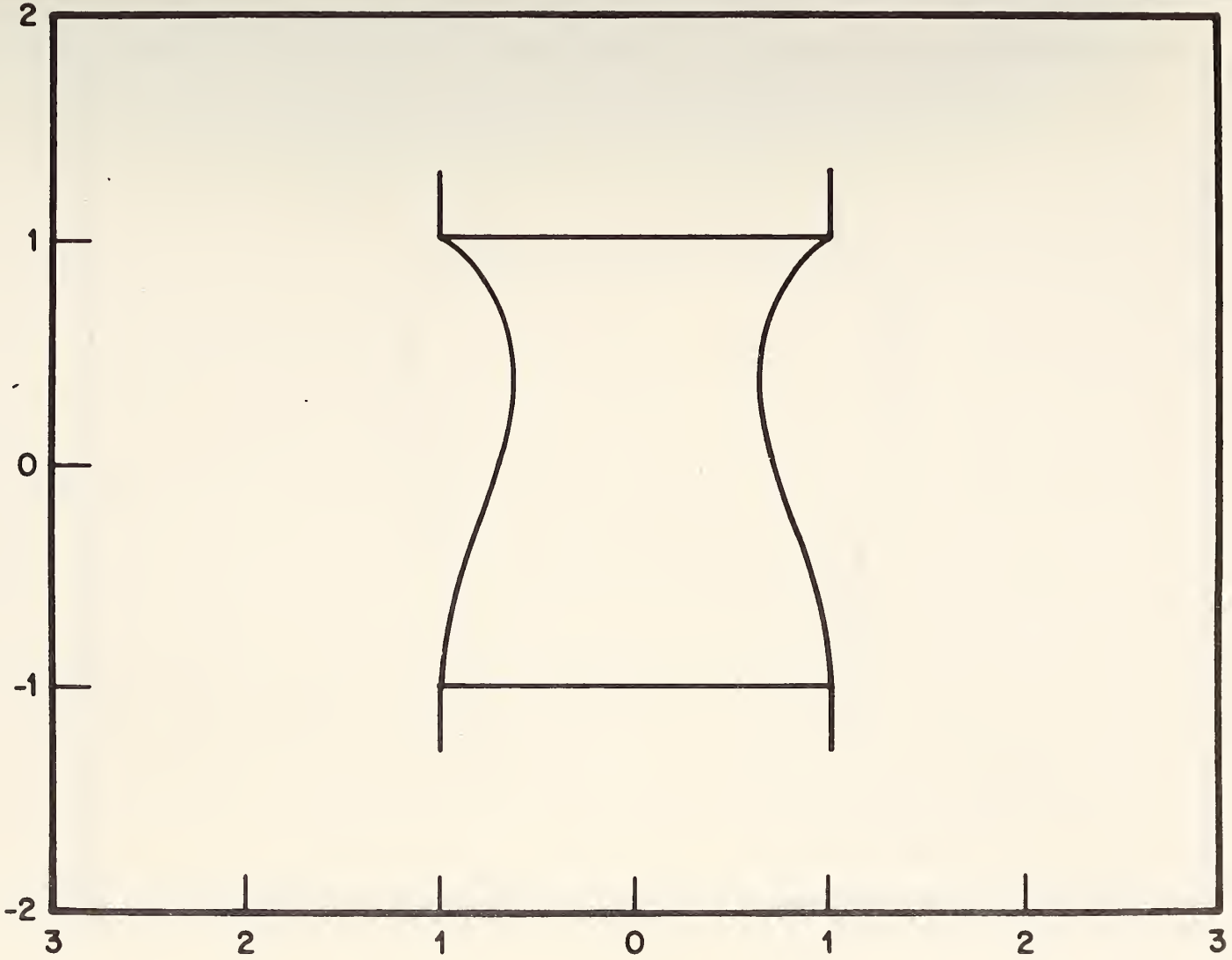

Fig. 12 Liquid zone for $R_u/R = 1.0$, $L/R = 2.0$, $\varepsilon_R = 0$, $\varepsilon = 1.25$ and $\phi_f = 0$. Compare with Fig. 11.

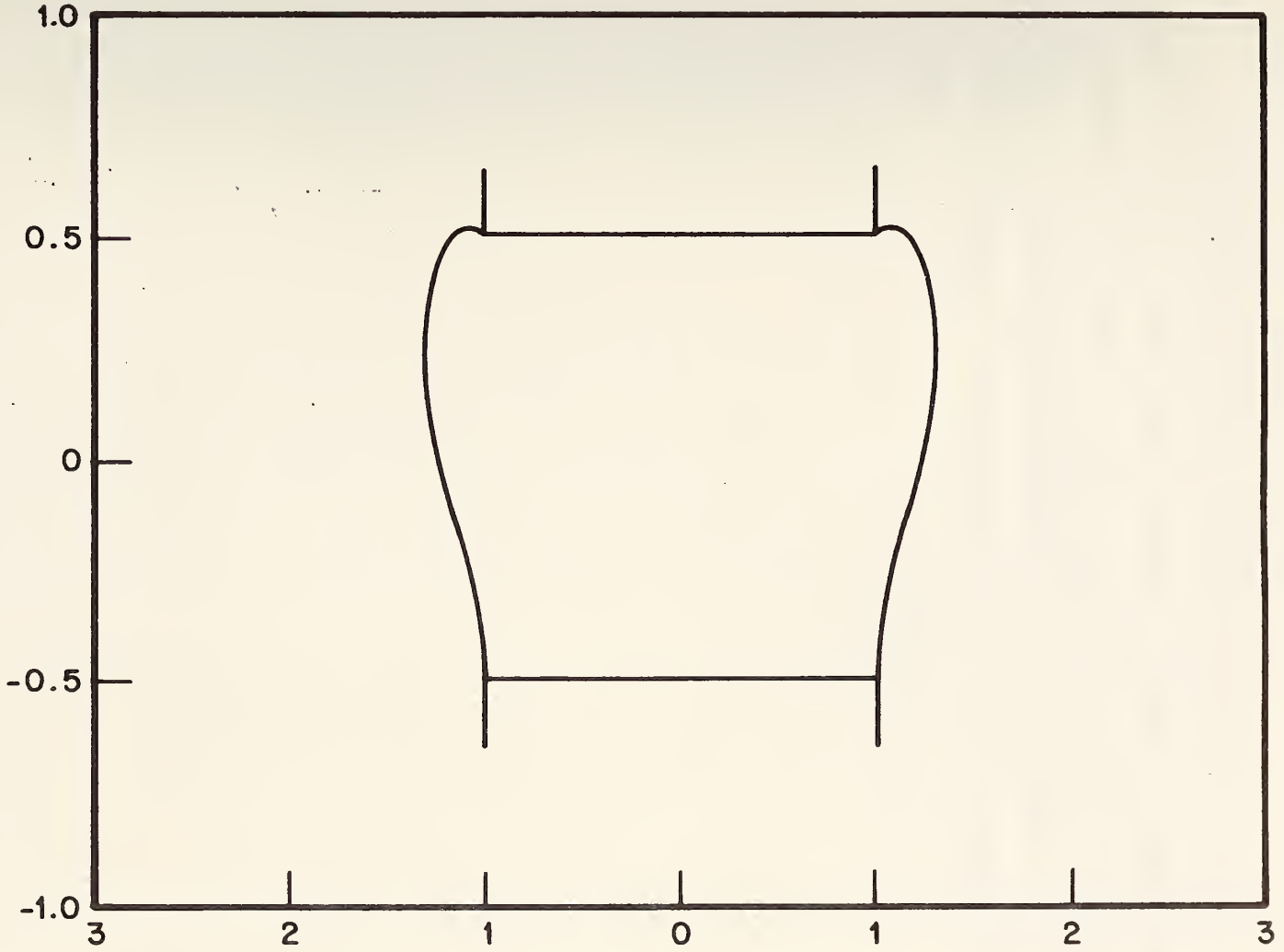

Fig. 13 Liquid zone for $R_u/R = 1.0$, $L/R = 1.0$, $\varepsilon_R = 0$, $\varepsilon = -7.13$ and $\phi_f = 0$.

Task 5

NBS personnel continue to consult extensively with NASA Headquarters and NASA field offices as required. We have visited Marshall SFC, Alabama on numerous occassions and have provided advice on many aspects of the Space Processing Program, including Shuttle Payloads. We continue our Space Processing Seminar at NBS.

National Aeronautics and Space Administration
Washington, D. C. 20546

Mr. F. L. Williams	Code ES	1 copy
Dr. J. H. Bredt	Code ES	4 copies

National Aeronautics and Space Administration
Johnson Space Center
Houston, Texas 77058

Mr. W. E. Rice	Code EA	2 copies
Mr. J. P. Loftus	Code AT	1 copy
Mr. J. A. Mason	Code DA	1 copy
Mr. E. J. Svreek	Code FM5	1 copy

National Aeronautics and Space Administration
George C. Marshall Space Flight Center
Marshall Space Flight Center, Alabama 35812

Mr. H. P. Gierow	Code PD-MP-DIR	1 copy
Mr. K. R. Taylor	Code PD-MP-T	2 copies
Mr. B. O. Montgomery	Code S&E-DIR	1 copy
Dr. W. G. Johnson	Code S&E-R-DIR	1 copy
Mr. R. E. Lake	Code S&E-R	1 copy
Mr. R. Schwinghamer	Code S&E-ASTN-M	1 copy
Dr. R. S. Snyder	Code S&E-ASTN-MTE	1 copy
Mr. E. C. McKannan	Code S&E-ASTN-MM	1 copy
Mr. R. C. Ruff	Code S&E-ASTN-MEV	1 copy
Miss M. H. Johnston	Code S&E-ASTN-MEV	1 copy
Mr. H. Wuenscher	Code S&E-PE-DIR	1 copy
Mr. I. C. Yates, Jr.	Code S&E-PE-A	1 copy
Mr. L. H. Berge	Code S&E-PE-A	1 copy
Mr. G. M. Arnett	Code S&E-SSL-TR	1 copy
Mr. T. C. Bannister	Code S&E-SSL-T	1 copy
Mr. M. C. Davidson	Code S&E-SSL-TR	1 copy
Mr. A. C. Krupnick	Code S&E-ASTN-MT	1 copy
Mr. W. B. McPherson	Code S&E-ASTN-MMM	1 copy
Mr. J. H. Hess	Code S&E-ASTN-MM	1 copy
Mr. L. L. Lacy	Code S&E-SSL-NP	1 copy
Mr. M. F. Nowakowski	Code S&E-QUAL-QT	1 copy
Dr. R. E. Allen	Code S&E-ASTN-MTM	1 copy
Mr. P. H. Rhodes	Code S&E-ASTN-MTE	1 copy
Mr. J. Bond	Code S&E-ASTN-MTE	1 copy
Mrs. B. R. Facemire	Code S&E-SSL-TR	1 copy
Mr. C. F. Schafer	Code S&E-SSL-TR	1 copy
Mr. B. R. Aldrich	Code S&E-PE-MXX	1 copy
Mr. A. Boese	Code S&E-PE-A	1 copy
Mr. R. A. Taylor	Code S&E-PE-MEI	1 copy
Mr. J. R. Williams	Code S&E-PE-M	1 copy
Mr. V. H. Yost	Code S&E-PE-MW	1 copy
Dr. M. P. L. Siebel	Code S&E-PE-DIR	1 copy

Jet Propulsion Laboratory
California Institute of Technology
4800 Oak Grove Drive
Pasadena, California 91103

Dr. C. H. Savage	Code 158-235	1 copy
Dr. M. M. Saffren	Code 183-301	1 copy
Dr. T. G. Wang	Code 183-401	1 copy
Dr. D. D. Elleman	Code 183-401	1 copy
Dr. J. W. Lucas	Code 180-700	1 copy

National Aeronautics and Space Administration
Langley Research Center
Hampton, Virginia 23665

Dr. L. T. Melfi, Jr.	Code 401A	1 copy
Mr. B. W. Cocke, Jr.	Code 401A	1 copy
Dr. R. A. Outlaw	Code 234	1 copy
Dr. J. P. Mugler	Code 215B	1 copy
Mr. J. D. DiBattista	Code 215B	1 copy
Mr. W. C. Ayers	Code 418	1 copy

National Aeronautics and Space Administration
Ames Research Center
Moffett Field, California 91103

Dr. J. A. Parker	Code SC	1 copy

Grumman Aerospace Corporation
Bethpage, New York 11714

Dr. C. H. Li — 1 copy

General Electric Company
Space Sciences Laboratory
P.O. Box 8555
Philadelphia, Pennsylvania 19101

Dr. R. T. Frost — 1 copy

European Space Research Organization
114 Avenue Charles de Gaulle
92 Neuilly, France

Dr. G. Seibert — 1 copy

Gesellschaft fur Weltraumforschung mbH
505 Porz-Wahn
Linder Hohe
German Federal Republic

Dr. A. Bewersdorff — 1 copy

NBS-114A (REV. 7-73)

U.S. DEPT. OF COMM. BIBLIOGRAPHIC DATA SHEET	1. PUBLICATION OR REPORT NO. NBSIR 77-1208	2. Gov't Accession No.	3. Recipient's Accession No.

4. TITLE AND SUBTITLE

NBS Space Processing Research

5. Publication Date: January 1977

6. Performing Organization Code

7. AUTHOR(S)

E. Passaglia & R. L. Parker

8. Performing Organ. Report No.

9. PERFORMING ORGANIZATION NAME AND ADDRESS

NATIONAL BUREAU OF STANDARDS
DEPARTMENT OF COMMERCE
WASHINGTON, D.C. 20234

10. Project/Task/Work Unit No.

11. Contract/Grant No.

12. Sponsoring Organization Name and Complete Address (Street, City State, ZIP)

NASA - Marshall SFC
Huntsville, Alabama

13. Type of Report & Period Covered Annual Report 1/76-12/76

14. Sponsoring Agency Code

15. SUPPLEMENTARY NOTES

Annual Report

16. ABSTRACT (A 200-word or less factual summary of most significant information. If document includes a significant bibliography or literature survey, mention it here.)

This report describes NBS work for NASA in support of NASA's Space Processing Program covering the period January 1, 1976 - December 31, 1976.

The results obtained for each task are given in detailed summaries in the body of the report. Briefly, in Task 1 - Crystal Perfection in Czochralski Growth - large nickel single crystals have been grown having dislocation densities as low as 400 lines / cm^2 as assessed by x-ray dynamical diffraction techniques. In Task 2 - Evaporative Purification of Ultra-High Purity Materials - Part A - it was determined that the use of sessile drops as a means of support for the study of molten alumina places severe restrictions on the type and validity of the data that can be obtained in view of temperature measurement and control problems encountered. In Part B, rates of evaporative purification were determined for Nb-Mo and for Mo-Zr alloys at elevated temperatures using R.F. levitation of molten drops. In Task 3 - Vapor Transport Synthesis and Crystal Growth - the growth of 1.5 cm diameter crystals of mercurous chloride crystals by a vapor Bridgman technique is described. In Task 4 - Melt Shape in Weightless Crystal Growth, thermocapillary forces on air bubbles in a viscous oil were measured, and the shape of axisymmetric liquid zones and their stability with respect to perturbations has been investigated numerically.

17. KEY WORDS (six to twelve entries; alphabetical order; capitalize only the first letter of the first key word unless a proper name; separated by semicolons)

Convection; crystal growth; crystal perfection; microgravity; purification; space processing.

18. AVAILABILITY

[X] Unlimited

[ ] For Official Distribution. Do Not Release to NTIS

[ ] Order From Sup. of Doc., U.S. Government Printing Office Washington, D.C. 20402, SD Cat. No. C13

[X] Order From National Technical Information Service (NTIS) Springfield, Virginia 22151

19. SECURITY CLASS (THIS REPORT)	21. NO. OF PAGES
Unclassified UNCLASSIFIED	114
20. SECURITY CLASS (THIS PAGE)	**22. Price**
UNCLASSIFIED	$5.50

USCOMM-DC 29042-P74